Unsupervised Domain Adaptation Through Inter-Modal Rotation for RGB-D Object Recognition

Nonlinear Dyn
https://doi.org/10.1007/s11071-024-09396-z

ORIGINAL PAPER

Parametric study for model calibration of a friction-damped turbine blade with multiple test data

Erhan Ferhatoglu · Daniele Botto · Stefano Zucca

Received: 23 October 2022 / Accepted: 5 February 2024

Abstract Model updating using multiple test data is usually a challenging task for frictional structures. The difficulty arises from the limitations of nonlinear models which often overlook the uncertainties inherent in contact interfaces and in actual test conditions. In this paper, we present a parametric study for the model calibration process of a friction-damped turbine blade, addressing the experimentally measured response variability in computational simulations. On the experimental side, a recently developed test setup imitating a turbomachinery application with mid-span dampers is used. This setup allows measuring multiple responses and contact forces under nominally identical macroscale conditions. On the computational side, the same system is modeled in a commercial finite element software, and nonlinear vibration analyses are performed with a specifically developed in-house code. In numerical simulations, the multivalued nature of Coulomb's law, which stems from the inherent variability range of static friction forces in permanently sticking contacts, is considered to be the main uncertainty. As the system undergoes vibration, this uncertainty propagates into the dynamic behavior, particularly under conditions of partial slip in contacts, thus resulting in response variability. A deterministic approach based on an optimization algorithm is pursued to predict the limits of the variability range. The model is iteratively calibrated to investigate the sensitivity of response limits to contact parameters and assembly misalignment. Through several iterations, we demonstrate how uncertain initial contact conditions can be numerically incorporated into dynamic analyses of friction-damped turbine blades. The results show a satisfactory level of accuracy between experiments and computational simulations. This work offers valuable insights for understanding what influences test rig response and provides practical solutions for numerical simulations to improve agreement with experimental results.

Keywords Model updating · Contact · Nonlinear vibration · Variability · Uncertainty

List of symbols

C	Damping matrix
K	Stiffness matrix
M	Mass matrix

E. Ferhatoglu · D. Botto (✉) · S. Zucca
Department of Mechanical and Aerospace Engineering, Politecnico di Torino, Corso Duca degli Abruzzi 24, 10129 Turin, Italy
e-mail: daniele.botto@polito.it

E. Ferhatoglu
e-mail: erhan.ferhatoglu@polito.it

S. Zucca
e-mail: stefano.zucca@polito.it

Present Address:
E. Ferhatoglu
Institute of Aircraft Propulsion Systems, University of Stuttgart, Stuttgart, Germany

Published online: 28 March 2024

$\mathbf{R}$	Residual vector
$\mathbf{f}_c$	Vector of contact forces
$\mathbf{f}_{exc}$	Vector of excitation forces
$\mathbf{m}$	Vector of multiplier coefficients
$\mathbf{q}$	Vector of generalized coordinates
F_{clamp}	Static clamping force
F_{exc}	Excitation force applied by shaker
$\|F_{exc}\|$	Fundamental harmonic amplitude of excitation force applied by shaker
h	Harmonic number
H	Maximum number of harmonics considered
i	Imaginary unit number, $\sqrt{-1}$
k_t	Contact stiffness in tangential direction
N	Normal load on contact elements
N_c	Number of contact points
R	Reaction forces measured by de-couplers
t	Time
t_{ini}	Initial time instant
T	Contact force in tangential direction
u	Relative motion in tangential direction
U_{pot}	Potential energy
v	Relative motion in normal direction
w	Slip displacement
α	Design angle of de-couplers
ΔW_{dis}	Dissipated energy
η	Loss factor
μ	Coefficient of friction
ω	Excitation frequency
θ	Design angle on dampers
ζ	Damping ratio
$\square^0$	Static component of $\square$
$\dot{\square}$	First time derivative of $\square$
$\ddot{\square}$	Second time derivative of $\square$
$\square_{min}$	Minimum of $\square$
$\square_{max}$	Maximum of $\square$
BC	Boundary condition
CF	Centrifugal force
LC	Load cell

1 Introduction

Friction is an inevitable phenomenon in jointed assemblies, occurring both intentionally and unintentionally depending on the specific application. In turbomachinery applications with underplatform dampers, friction is intentionally employed in bladed disks to reduce excessive vibration amplitudes and prevent high cycle fatigue failure of aeroengines [1–4]. Conversely, in structures with bolted joints, unintentional friction arises when two or more bodies come into contact during operation, leading to relative motion and sliding [5–7]. Over the past four decades, significant efforts have been devoted to the prediction of the nonlinear dynamic behavior of structures subject to friction in these fields.

State-of-the-art numerical solvers have demonstrated remarkable accuracy in predicting dynamic behavior under well-defined macroscale conditions. However, challenges arise when uncertain test conditions are encountered at micro scales. Such uncertainties contribute to variations in system characteristics and test data, leading to difficulties in updating procedures of the nonlinear models. In the last years, the joint mechanics and turbomachinery communities have highly focused on the variability and repeatability of nonlinear dynamics in assemblies. The primary concern revolves around identifying uncertainties present in contact interfaces [8–10] and effectively representing them in numerical simulations. This issue poses a challenging problem particularly in friction-damped turbine blades: the tuning of numerical models using multiple test data to better predict the nonlinear dynamics of structures. Throughout the paper, the term *multiple* refers to several sets of measurement data obtained under nominally identical macroscale conditions, but in different experiments.

A common practice in the context of model updating involves fine-tuning the contact parameters [11–17]. This approach is feasible for a single set of contact parameters in cases where the effects of uncertainties on the system behavior variability are negligible. Once the scattering of the experimental data increases, an uncertainty band that accounts for non-repeatability is necessary in computational results. To establish such an uncertainty band, several studies have addressed uncertainties using stochastic approaches and subsequently propagating them to system behavior [18–21]. Monte Carlo Simulations (MCS) [22] are widely used due to their robustness. However, MCS are computationally expensive since it requires a large number of samples. Reduced order models and surrogate modeling approaches are popular techniques to increase the computational efficiency. Butlin et al. [23–25] also consider the functional form of constitutive laws as uncertain and

employ probabilistic and/or constrained optimization techniques to determine response bounds.

Present study considers the uncertainty arising from the multivalued characteristics of Coulomb's law, particularly in static friction forces of permanently sticking contacts. To better illustrate this uncertainty, consider a simplified example: a single degree-of-freedom grounded mass-spring system, with the generalized coordinate x, subject to friction. The governing equation for this system, with unit mass, is given by $\ddot{x} + kx + T = 0$, where k represents the spring stiffness and T represents tangential friction force. For static equilibrium, we know that $\ddot{x} = 0$, and Coulomb's law states that $|T| < \mu N$, indicating $T \in (-\mu N, \mu N)$. This condition implies that the static friction force of a sticking contact can assume an infinite number of values within a range. In other words, the system's equilibrium lies within the interval of $(-\mu N/k, \mu N/k)$. Once an initial condition is selected from this interval, the solution corresponds to one of the infinitely many points, and the system is considered to be in equilibrium. In reality, the actual tangential friction force, and hence static equilibrium, is determined by one particular loading history experienced by the system, which is mostly unknown. Loading history can be arbitrarily different, for instance, due to different application patterns of initial pre-loads and the subsequent load history, which may involve quasi-static loading, random impulsive perturbations and dynamic loading across various time scales. Consequently, static friction force of permanently sticking contacts can have a memory and can take a value within the variability range whose limits are imposed by Coulomb's law. The variability range is further depicted in Fig. 1 for a more generic case with time-dependent tangential and normal contact forces.

The hysteretic uncertainty in static friction forces of fully stuck contacts has been first demonstrated in the contact mechanics community, particularly on quasistatic contact problems with friction [26, 27]. Several researchers have focused on predicting shakedown limits to determine the extent to which contacts retain the memory [28–31]. In the case of vibrating systems, the long-term behavior is influenced by whether this memory is preserved or lost. In cases where all contacts experience recurrent sliding and/or lift-off without any permanent sticking, the system eventually loses its memory, leading to a single

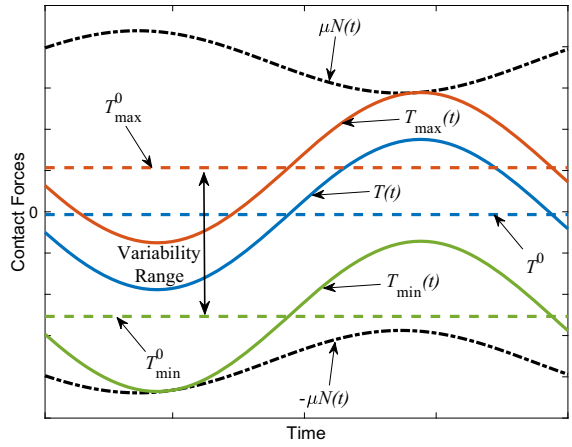

Fig. 1 Contact forces and variability range of static tangential force in a permanently sticking contact

long-term behavior. When at least one but not all contacts display permanent sticking, multiple long-term behaviors can occur if the contacts are coupled, meaning that the normal forces are influenced by the tangential forces and vice versa. This coupling can arise due to structure geometry, such as contacts aligned at an angle (geometric coupling), or due to the elastic coupling between the normal and tangential directions of different contacts during vibrations. In the field of structural dynamics, Yang and Menq [32, 33] were the first to recognize that the set of multiple static equilibria due to different initial conditions of static friction forces can introduce variability in the steady-state forced response of friction-damped structures. Over the past two decades, several studies [34–39] have shown the possibility of multiple responses in friction-damped turbine blades due to this phenomenon. The effects of such variability on the dynamics of the system cannot be disregarded, as it can result in significant differences of up to 20% in resonance frequency and 300% in response amplitudes for nominally identical cases [38, 39].

In the context of this uncertainty, researchers have developed deterministic methods for the characterization of uncertainty bands. For example, in [32], the authors utilized geometric relations in damper kinematics to calculate upper and lower limits in the response. Similarly, the authors of [40] emphasized the use of maximum and minimum tangential forces to estimate limiting cases with a simpler yet effective approach. Other methodologies, which are based on nonlinear modes [41] and optimization algorithms

[42], have been developed to predict the boundary range of variability. The latter has also been applied to realistic cases, such as an academic turbine blade coupled with underplatform dampers [43], and its efficacy has been validated through test data measured on turbine blades. It should be noted that in order to improve the accuracy of matching the computationally obtained variability range with corresponding experimental measurements, model calibration may still be necessary for the aforementioned approaches.

The objective of this work is to demonstrate how a friction-damped turbine blade model can be iteratively calibrated using multiple test data with a parametric study. As the main source of the response variability, the epistemic uncertainty present in static friction forces of permanently sticking contacts is taken into account. A key contribution of this paper is the adoption of a non-probabilistic strategy for the model updating process, incorporating an optimization algorithm to estimate the limits of the variability range. The model is iteratively tuned with respect to the sensitivity of limits to both contact parameters and the alignment of the test setup. Substantial effort is dedicated to calibrating the model for both linear and nonlinear analyses. It is shown that the computational and experimental results match with a negligible amount of error after a thorough updating process of the model.

The paper is organized as follows. Section 2 describes the test setup, measurement procedures and presents the test data. Section 3 explains the computational background utilized in the numerical side of the study. In Sect. 4, the comparison of the experimental and computational results is illustrated to show how the model calibration is performed. Section 5 concludes the study and summarizes the key points.

2 Test rig: a turbine blade with mid-span dampers

The experimental campaign of the current study involves a newly designed test rig that imitates turbine blades coupled with mid-span dampers. The test setup has been extensively described in [44]. To present an understanding of the experimental setup, we provide a brief overview of its main components and measurement procedures.

2.1 Main components

The complete assembly of the test rig is depicted in Fig. 2a. Central and side blocks serve as bulky host entities, and they are securely fastened to the table. The side blocks carry additional components to measure contact forces. The test rig consists of three

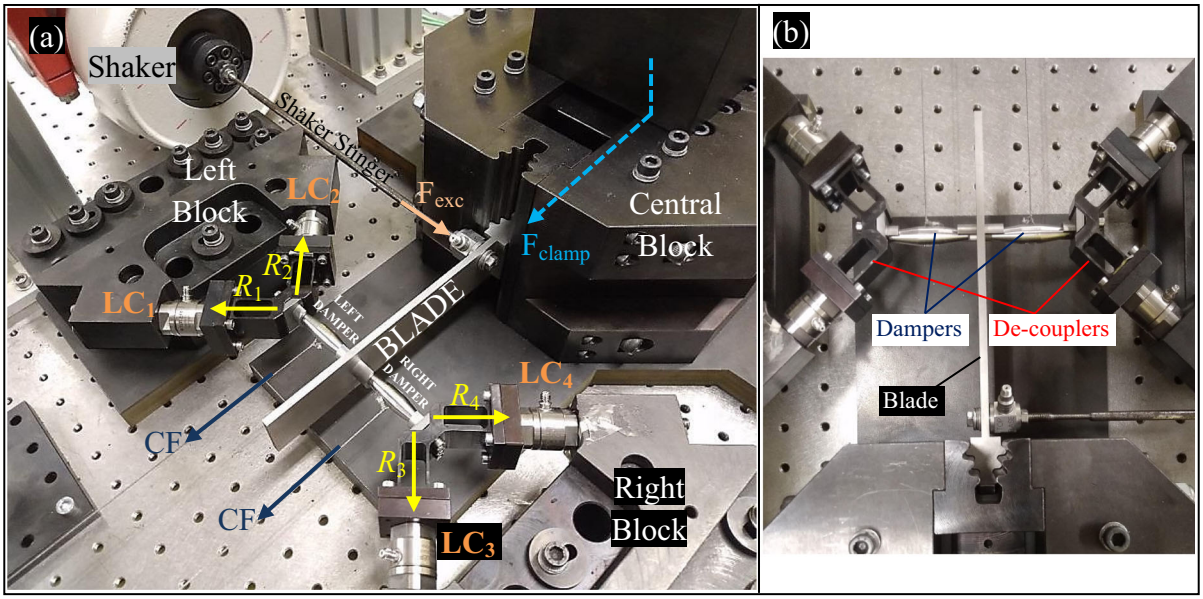

Fig. 2 **a** Entire assembly of the test setup, **b** Top view of main subcomponents: one blade, two dampers and two de-couplers

main subcomponents: a blade, two bi-conical dampers, and two L-shaped de-couplers (see Fig. 2b).

1. The blade is a slender beam specifically developed for academic purposes and designed similarly to those used in industrial applications [45, 46]. It is fixed to the central block through a clamping mechanism that ensures a substantial clamping force (F_{clamp}) on the blade's base. This mechanism minimizes the potential friction at the blade root. The blade is excited with a harmonic force, $F_{exc}(t) = |F_{exc}| \cos(\omega t)$, by an electromagnetic shaker that is attached to the nearby of the root with a stinger.
2. Dampers are positioned between the blade and de-couplers. The design of the dampers is also based on the geometry of their industrial counterparts [45, 46], considering shape, dimensions, and functionality. A line contact is ensured with specifically machined conical slots on both the blade and the L-shaped de-couplers (see Fig. 2b). Each damper is subjected to a static pulling force generated by dead weights. These pre-loads emulate the centrifugal force (CF) during real working conditions, resulting from the rotational speed of the bladed disk.
3. The de-couplers are connected to two blocks (left and right) via load cells (LC). Their main function is the separation of the contact forces exerted by the dampers into two orthogonal reaction forces (R). These reaction forces are then measured by the load cells.

2.2 Measurement procedures

The tests are conducted using force-controlled stepped-sine frequency sweeps. In addition to monitoring the response of the blade, measurements are taken for the reaction forces and relative displacement between the right damper and the blade.

Figure 3a shows the free body diagram of the de-couplers, with T and N representing the tangential and normal contact forces, respectively. The reaction forces measured by load cells are denoted as R_3 and R_4. The force balance equations can be expressed in horizontal and vertical directions as

$$\begin{aligned} T\cos(\theta) + N\sin(\theta) - R_3\cos(\alpha) - R_4\cos(\alpha) &= 0 \\ T\sin(\theta) - N\cos(\theta) + R_3\sin(\alpha) - R_4\sin(\alpha) &= 0, \end{aligned} \tag{1}$$

where α and θ are 45° and 8.53°, respectively. Given that the reaction forces are already measured, contact forces can be easily obtained by solving the coupled Eq. (1). Similarly, the force equilibrium on the damper is also depicted in Fig. 3b. T' and N' denote the contact

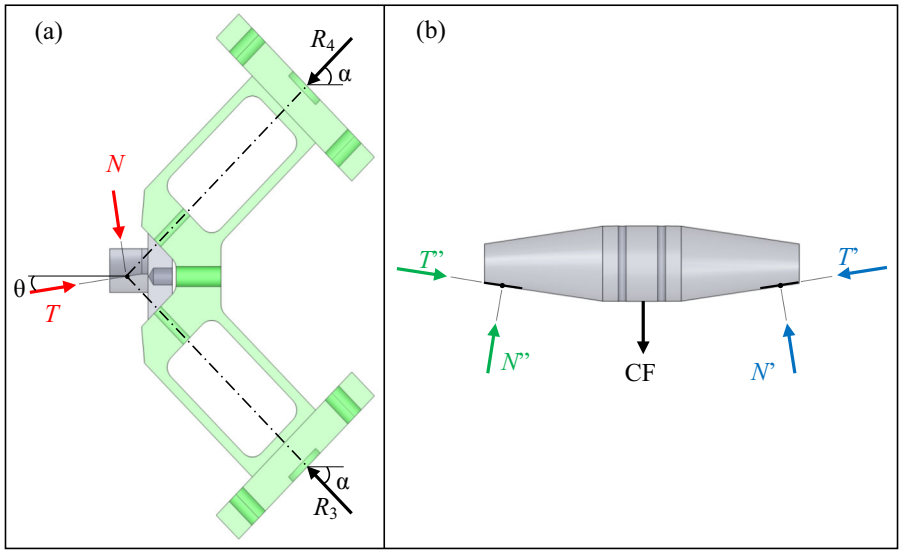

Fig. 3 Force equilibrium at the right side. **a** On the de-coupler: Load cells are replaced by the measured reaction forces (R_3 and R_4). Damper is replaced by contact forces (T & N). **b** On the damper: The force de-coupler is replaced by contact forces (T' & N'). The blade is replaced by contact forces (T'' & N'')

forces at the de-coupler side of the damper and are equal to T and N in magnitude. T'' and N'' also represent contact forces at the blade side. The balance equations can then be expressed as

$$\begin{aligned} T''\cos(\theta) + N''\sin(\theta) - T'\cos(\theta) - N'\sin(\theta) = 0 \\ -T''\sin(\theta) + N''\cos(\theta) - T'\sin(\theta) + N'\cos(\theta) - \mathrm{CF} = 0 \end{aligned}. \tag{2}$$

In Eq. (2), the inertia of the damper is considered negligible due to low mass of the damper.

The response of the blade was measured by an accelerometer attached to the blade tip, as shown in Fig. 4a. To construct the hysteresis cycles, a differential laser was also utilized to measure the relative displacement between the blade and the damper. It is important to note that due to space limitations in the test campaign, precise measurement of the relative displacement was challenging. Figure 4a and 4b illustrate the laser points and the positions of the laser heads, respectively. One of the laser heads is directed toward a point near the contact slot of the blade, while the other head is pointed on top of the damper. To facilitate the measurement, a reflective tape was attached using an additional indenter wrapped around the damper, as the middle section of the damper is perfectly circular and lacks any indentation to reflect the light back to the laser. Furthermore, one of the laser heads was inclined at an angle of approximately 12°–15° to obtain measurements. It is worth underlining that the primary objective of this measurement was to gain initial insights into the order of magnitude of contact parameters, and the final values utilized in numerical simulations are iteratively calibrated, as elaborated in Sect. 4.

2.3 Test results

The comprehensive discussion on the experimental data obtained from the test rig employed in this study can be found in [44]. For the sake of completeness, we present the most significant test results in this subsection, as they will be utilized in the model calibration process in Sect. 4.

2.3.1 Linear characteristics of the stand-alone blade

We initially investigated the linear behavior of the blade using stepped-sine frequency sweep tests focused on the vicinity of the lowest frequency mode. Specifically, we considered the stand-alone blade configuration without dampers. In this setup, the blade is firmly secured to the central host block through the application of a substantial static load (F_{clamp}, see Fig. 2a). To investigate the impact of potential damping at the blade root on the linear characteristics, the blade was excited using five different amplitudes of harmonic excitation. Figure 5a presents the normalized response of the blade for increasing levels of excitation. It is evident that the responses align closely with each other, except for the case with the lowest excitation amplitude. This slight deviation suggests a minor contribution of damping from the blade root. It is important to note that completely preventing damping at the blade root is practically impossible, regardless of the magnitude of the applied clamping force. Furthermore, once the dampers are engaged, the vibration amplitudes will significantly decrease compared to the free blade scenario. Consequently, the primary source of damping will predominantly arise from the contacts between the blade and the dampers.

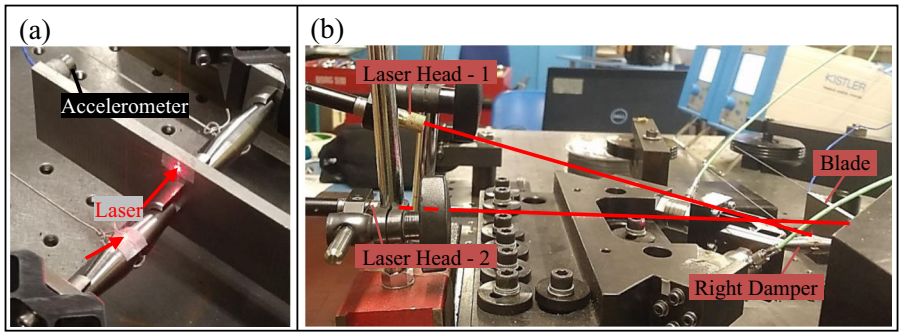

Fig. 4 **a** Laser points for the measurement of relative displacement between the blade and the damper, **b** back view for the position of laser heads

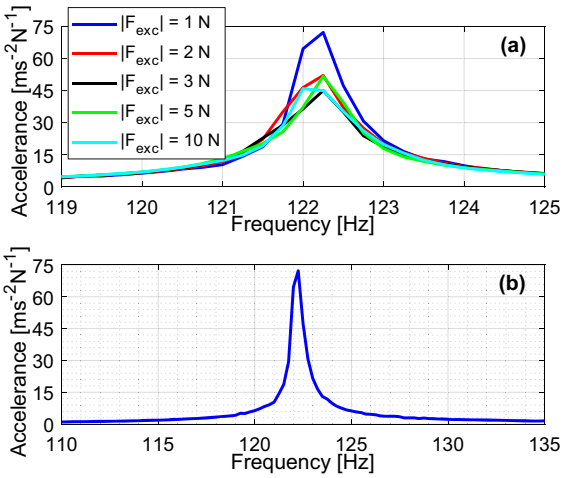

Fig. 5 Linear response of the blade without dampers: **a** for cases with five different excitation amplitude levels, **b** over a wider frequency range for the case with $|F_{exc}|$= 1 N

Hence, based on the results presented in Fig. 5a, it is reasonable to conclude that the damping at the blade root can be considered negligible. Figure 5b displays the response of the free blade over a wider frequency range. It shows that the mode of interest is well separated, with a measured natural frequency of 122.25 Hz.

2.3.2 *Measurement of multiple nonlinear responses and contact forces*

Coupled blade-damper configuration is tested around the frequency range near to the lowest frequency mode of the stuck system. The dampers are engaged to the blade by applying pre-loads through dead weights, as explained in SubSect. 2.1. In this study, the nominal pre-load value on the damper was set at 5.6 kg for all tests.

Vibration tests are performed by keeping all user-controlled inputs identical in the macroscale test environment. To measure multiple vibration responses and contact forces in different tests, the loading history of the system was deliberately altered prior to the start of each test. The ultimate strategy was to obtain the maximum number of different arbitrarily defined loading histories before each run, while maintaining identical inputs across all runs during the tests. In this way, the range of the variability in the data is increased as extensively as possible. This was accomplished by implementing various loading and unloading sequences. For instance, for certain tests, the pre-loads on the damper were initially increased or decreased to an arbitrary value different from the nominal one utilized during the tests. Shortly before the start of each test, the pre-loads were then set to the nominal value. In other cases, consecutive tests were performed with the dampers remaining loaded, while in different tests, the dampers were completely unloaded and then reloaded. Furthermore, some tests were performed with forward frequency sweeps, while others were carried out with backward sweeps. In the experiments, the data variability is examined for four different subcases, each driven by one of the four different excitation levels: 1 N, 3 N, 5 N, and 10 N.

Figure 6 shows the comprehensive view of the experimentally obtained multiple responses of the blade. The data exhibit a significant degree of non-repeatability, varying by up to a factor of 2 particularly in amplitude levels of the case with 5 N excitation level. Figure 7 also presents the multiple contact forces on the de-coupler sides of the left and right dampers. The data are presented at resonance frequencies of four demonstrator test cases, and both dynamic and static components are depicted in each subfigure. In contrast to the nonlinear response, the degree of variability observed in the contact forces is relatively smaller. These experimental results will serve as the reference data for the subsequent model calibration process discussed in Sect. 4.

It is also worth highlighting that across all excitation levels, a disparity exists in the static normal force values between the left and right dampers. This difference indicates a misalignment present in the assembly, as the static pre-load introduced by the dead weights is expected to be equally shared by both sides of the dampers under the assumption of an ideal condition with perfect symmetry. Specifically, with a pre-load of 5.6 kg, each side is expected to receive a static normal load of approximately 27.5 N. However, it is observed that the left damper shows an offset of around 7 N. Further, no additional measurements were conducted to visualize the actual distribution of static forces on contact interfaces. Consequently, the misalignment of the dampers and the application of pre-loads will be correspondingly addressed during the calibration process.

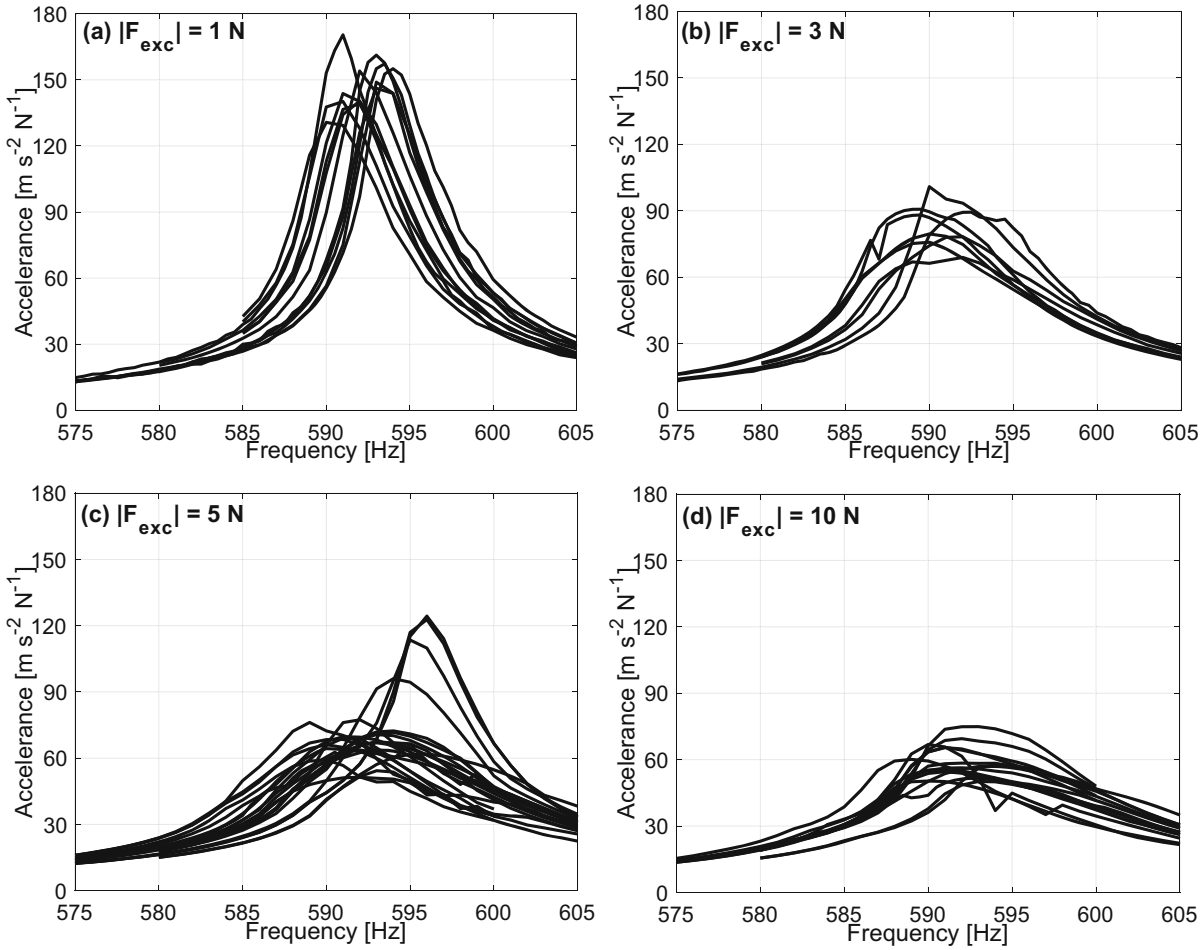

Fig. 6 Multiple nonlinear responses of the blade for different excitation amplitude levels

3 Computational background

In this section, the numerical background is presented for the deterministic simulations of limits of multiple dynamic responses and contact forces.

3.1 Finite element model and governing equations

The components of the test setup are meshed with a commercial finite element software. Since the central block and side blocks are quite bulky, they are assumed to be rigid and are thus excluded from the model. Additionally, the load cells and auxiliary components are unified to the de-couplers, as they are tightly bolted together. As a result, the model consists of five distinct bodies: the blade itself, two dampers, and two de-couplers. The finite element model of the assembly is depicted in Fig. 8. In the model, the blade is clamped at the root, while the de-couplers are fixed at the far ends of the load cells. The dampers, on the other hand, are free from any imposed boundary conditions. 3D 20-node solid elements are used to mesh all the components, resulting in a total of approximately 2.5 million elements. To obtain reduced-order system matrices, the Craig-Bampton approach [47] is employed in the reduction process. Generalized coordinates of many physical nodes (including excitation, static pre-load, response monitoring and contact nodes) as well as 150 modal coordinates are retained as the master degrees of freedom in the model. It should be noted that the model shown in Fig. 8 is the final version of the calibration procedure that will be elaborated in Sect. 4.

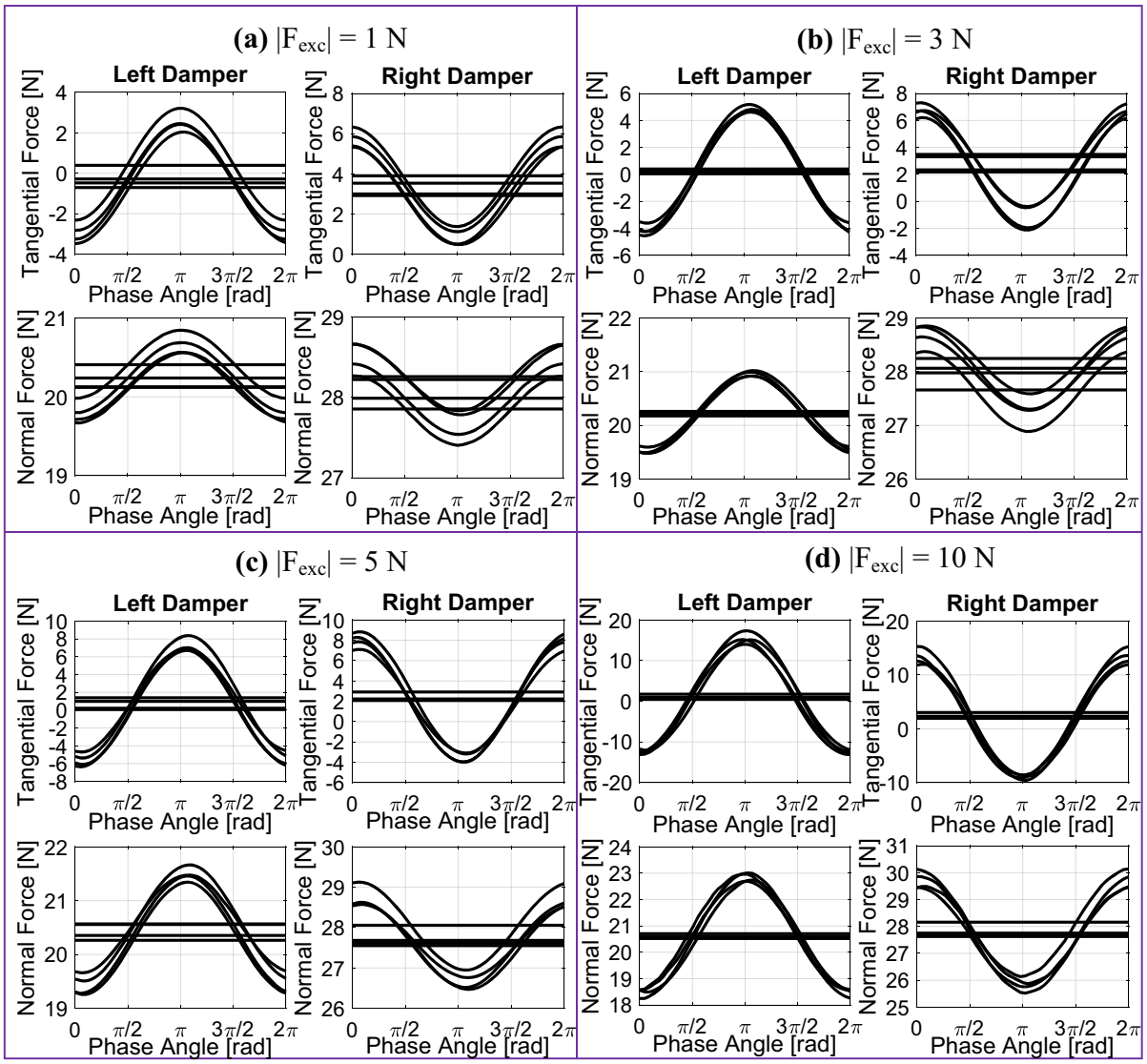

Fig. 7 Multiple contact forces on dampers for different excitation amplitude levels

Equation (3) is the generic equation of motion that can be written with the reduced-order system matrices, i.e., $\mathbf{M}$, $\mathbf{C}$ and $\mathbf{K}$, generalized coordinates, i.e., $\mathbf{q}(t)$, internal contact forces, i.e., $\mathbf{f}_c(\mathbf{q}, \dot{\mathbf{q}}, t)$, and external forcing, i.e., $\mathbf{f}_{exc}(t)$ as

$$\mathbf{M}\ddot{\mathbf{q}}(t) + \mathbf{C}\dot{\mathbf{q}}(t) + \mathbf{K}\mathbf{q}(t) + \mathbf{f}_c(\mathbf{q}, \dot{\mathbf{q}}, t) = \mathbf{f}_{exc}(t). \quad (3)$$

In this study, the blade is harmonically forced, and its steady state solution is sought using Harmonic Balance Method [48]. Hence, the forcing, nonlinear forces and the response can be written with their harmonic components as

$$\mathbf{f}_{exc}(t) = \Re\left(\sum_{h=0}^{H} \hat{\mathbf{f}}_{exc}^{h} e^{ih\omega t}\right),$$
$$\mathbf{f}_c(\mathbf{q}, \dot{\mathbf{q}}, t) = \Re\left(\sum_{h=0}^{H} \hat{\mathbf{f}}_c^{h} e^{ih\omega t}\right), \quad \text{and} \quad (4)$$
$$\mathbf{q}(t) = \Re\left(\sum_{h=0}^{H} \hat{\mathbf{q}}^{h} e^{ih\omega t}\right).$$

In Eq. (4), $\hat{\mathbf{f}}_{exc}^{h}$, $\hat{\mathbf{f}}_c^{h}$ and $\hat{\mathbf{q}}^{h}$ represent the complex amplitude vectors of the h^{th} harmonics. H is the number of harmonics considered in the expansion. i

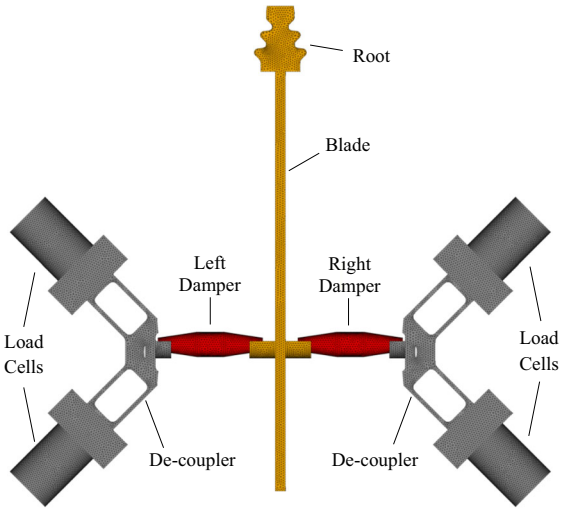

Fig. 8 Finite element model of the assembly

and ω denote the unit imaginary number and excitation frequency, respectively. To obtain the governing algebraic equations in the frequency domain, Eq. (4) can be inserted into Eq. (3) and the final set can be obtained as

$$\left(-(h\omega)^2\mathbf{M} + \mathrm{i}h\omega\mathbf{C} + \mathbf{K}\right)\hat{\mathbf{q}}^h + \hat{\mathbf{f}}_{\mathrm{c}}^h = \hat{\mathbf{f}}_{\mathrm{exc}}^h \quad (h = 0, 1, \cdots, H). \tag{5}$$

As mentioned in Sect. 2.1, the mating pairs of the test setup are deliberately designed to establish contact lines in the friction interfaces. This is achieved through the eccentric circular geometry of the dampers and corresponding contact surfaces of the contact pads and the blade, as depicted in Fig. 9. For each pair, seven contact points are selected.

In this study, the normal contact force, $N(t)$, is governed by a linear-elastic unilateral law that can be explicitly expressed as

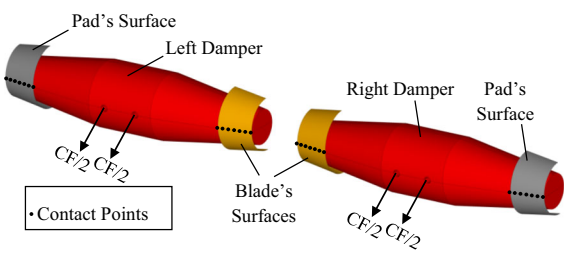

Fig. 9 Contact regions of the dampers with seven points selected on each mating surface

$$N(t) = \begin{cases} k_n v(t) & v(t) > 0, \text{ in contact} \\ 0 & v(t) \leq 0, \text{ lift - off} \end{cases}, \tag{6}$$

where $v(t)$ and k_n represent the relative displacements and contact stiffness value in the normal direction, respectively. The tangential contact force is governed by the elastic Coulomb's law. The friction force can be expressed with the differential form as

$$\mathrm{d}T(t) = \begin{cases} k_t \mathrm{d}u(t) & |T(t) + k_t \mathrm{d}u(t)| \leq \mu N(t), \text{ in stick} \\ 0 & |T(t) + k_t \mathrm{d}u(t)| > \mu N(t), \text{ in slip} \end{cases}. \tag{7}$$

Herein, $T(t)$ is the tangential contact force, k_t is the tangential contact stiffness and $u(t)$ represents the relative displacement in the tangential direction. μ represents the coefficient of friction in the contact. Due to hysteretic effects, the explicit form of $T(t)$ in terms of $u(t)$ and $\dot{u}(t)$ is not directly available. To address this phenomenon, in this study, we utilize the Jenkins-type point contact model (see Fig. 10), which incorporates an additional internal variable known as slip displacement ($w(t)$). The slip displacement represents a hypothetical coordinate defining the position of the slider within the contact element. Its value is constant when the contact is in the stick state ($\dot{w}(t) = 0$) and changes as the contact slips. This coordinate is treated implicitly within the harmonic balance approach, i.e., it is not represented as a truncated Fourier series. In this study, the complex amplitudes of the nonlinear forces are computed using the alternating time–frequency approach [49] with the well-known predictor–corrector scheme [50], where $T(t)$ is initially predicted using an estimated value of $w(t)$ and then corrected according to Coulomb's law. This prediction-correction procedure continues until

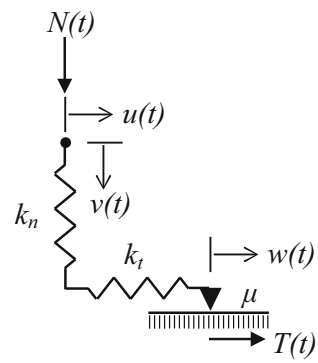

Fig. 10 Jenkins-type point contact element

the system reaches a steady state with periodicity conditions, typically requiring at least two periods. The tangential contact force can then be expressed by the following expression

$$T(t) = \begin{cases} k_t[u(t) - w(t)] & \text{in stick} \\ \mu N(t)|\dot{w}(t)|/\dot{w}(t) & \text{in slip} \\ 0 & \text{lift - off} \end{cases}, \tag{8}$$

where w is unknown at the initial loading instant, and its actual value depends on the loading history. In the literature, it is commonly assumed that the initial slip displacement of contacts is zero, although the actual value may differ. However, in this study, the initial slip displacements of contacts are considered uncertain, and their limit values are computed within an optimization algorithm together with the response limits.

3.2 Response variability and computation of limits with an optimization algorithm

The uncertainty in slip displacements of sticking contacts and consequently the tangential forces can lead to significant variability in the nonlinear response of turbine blades. To illustrate this phenomenon, consider Eq. (5) for two identical but separate test cases that have nominally same inputs but different loading histories. In this scenario, the system matrices ($\mathbf{M}$, $\mathbf{C}$ and $\mathbf{K}$) and forcing parameters ($\hat{\mathbf{f}}^{\mathrm{h}}_{\mathrm{exc}}$, h and ω) are identical for both cases in Eq. (5). Also assume that both systems exhibit partial slip motion, where some contacts are fully stuck while others experience stick–slip behavior, and there is a normal-tangential coupling among contacts. It was shown that the static components of contact forces, $\hat{\mathbf{f}}^0_c$, can take different values within a range for fully stuck contact points based on the loading history. Consequently, $\hat{\mathbf{f}}^0_c$ varies between the two cases, leading to different system responses, $\hat{\mathbf{q}}^h$, due to the coupling present in Eq. (5).

In this study, we computationally predict the limits of experimentally measured multiple responses using a numerical approach based on an optimization algorithm developed in [41]. The algorithm aims to minimize/maximize an objective function, represented by the system's loss factor, (η), which quantifies the damping capability of the system. Minimization of the loss factor is employed to determine the upper limit of the response, while maximization is used to compute the lower limit. The optimization problem is given as:

$$\begin{array}{ll} \text{minimize/maximize} & \eta \\ \text{with respect to} & [(\hat{\mathbf{q}}^h)^{\mathrm{T}}, \mathbf{m}^{\mathrm{T}}]^{\mathrm{T}}, \\ \text{subject to} & \mathbf{R} = \mathbf{0} \end{array} \tag{9}$$

where the loss factor is defined as the ratio between the total dissipated energy in the system, ΔW_{dis}, and the maximum stored energy, U_{pot}, [51, 52], i.e.,

$$\eta = \frac{\Delta W_{\mathrm{dis}}}{2\pi U_{\mathrm{pot}}}. \tag{10}$$

In Eq. (9), $\mathbf{m}$ is the vector of multiplier coefficients, representing the ratio of the initial tangential force to Coulomb's limit. Coefficients are implicitly defined for each contact element as

$$T_n(t_{\mathrm{ini}}) = m_n \times \mu N_n(t_{\mathrm{ini}}) \qquad (n = 1, 2, \cdots, N_{\mathrm{c}}), \tag{11}$$

where N_{c} is the number of contact elements. In this way, the uncertainty in initial tangential forces is addressed in the solution algorithm by considering each m_n as an unknown. t_{ini} represents the initial time instant in the predictor–corrector scheme. $\mathbf{R}$ denotes the residual of Eq. (5) and can be obtained as

$$\mathbf{R} = \hat{\mathbf{q}}^h + \boldsymbol{\alpha}^h\left(\hat{\mathbf{f}}^h_{\mathrm{c}} - \hat{\mathbf{f}}^h_{\mathrm{exc}} - \mathbf{K}_{\mathrm{c}}\hat{\mathbf{q}}^h\right) \qquad (h = 0, 1, \cdots, H). \tag{12}$$

$\boldsymbol{\alpha}^h$ is the receptance corresponding to each harmonic, i.e., $\boldsymbol{\alpha}^h = \left(-(h\omega)^2\mathbf{M} + \mathrm{i}h\omega\mathbf{C} + \mathbf{K}_{\mathrm{stuck}}\right)^{-1}$, where $\mathbf{K}_{\mathrm{stuck}}$ is the stiffness matrix of fully stuck linear configuration. Lastly, $\mathbf{K}_{\mathrm{c}} = \mathbf{K}_{\mathrm{stuck}} - \mathbf{K}$. The optimization technique utilized in this study is the interior point method [53, 54], and it is employed with *fmincon* built-in function of Matlab. The gradients are numerically calculated with forward finite difference method. It is worth mentioning that the optimization algorithm utilized in this study has been successfully demonstrated and applied in [42] with highly accurate results and reasonable computational cost. There may also be other optimization methods that could be more suitable for different applications. Evaluating and comparing different strategies, however, is beyond the scope of this study. In achieving the objectives of the calibration process presented in this study, the *fmincon*

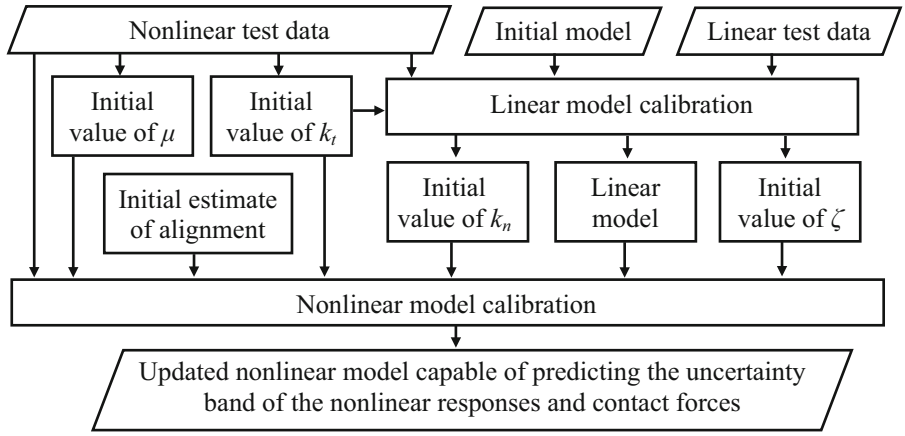

Fig. 11 Overview of the entire calibration process

algorithm with the interior-point method was deemed sufficient and effective.

4 Correlation of the results and model calibration

This section presents the calibration procedure for both linear and nonlinear models. The linear model refers to the model of the assembly without accounting for friction in contact interfaces, whereas the nonlinear model additionally incorporates frictional interaction through contact elements. The ultimate objective of this study is the parametric calibration of the nonlinear model for the prediction of limits of multiple nonlinear responses and contact forces. Several iterations are performed to achieve the best possible agreement between the computational results and their corresponding experimental counterparts. Throughout these iterations, all the steps taken to achieve the most accurate results are explained in the subsequent sections, including those that result in mismatched outcomes, in order to provide insights into the effective and ineffective practices during the model updating procedure. By detailing both the successful and unsuccessful outcomes, this study highlights the recommended approaches as well as the pitfalls to avoid when updating the model.

It is also worth underlining that the primary objective of the designed test rig is to measure and quantify the variability in the nonlinear response and contact forces. While the test rig is not specifically built for the characterization of the contact parameters, efforts have been made to estimate initial values of the contact parameters based on the available data. As a result, before discussing the calibration of the nonlinear model, estimation of the initial values of the contact parameters and the calibration of the linear model are presented. These procedures will be presented separately, and an overview of the entire calibration process is given in Fig. 11.

4.1 Estimation of initial values for tangential contact stiffness and coefficient of friction

The initial estimation of the tangential contact stiffness (k_t) and friction coefficient (μ) is based on the measured hysteresis cycles and contact force ratio, respectively. To estimate k_t, two arbitrary cases with excitation levels of 1 N and 10 N are considered, as illustrated in Fig. 12a. In the 1 N case, a peak-to-peak straight line is plotted, while in the 10 N case, the stick region is approximated with a manually drawn line. The slope of both lines represents the value of k_t, which is found to be 11.5 N/μm. However, it should be noted that the measured relative displacement value is not entirely accurate, and the actual value is greater due to the inclination of the laser heads (see Fig. 4). Consequently, the actual value of k_t is considered to be lower than the estimated value of 11.5 N/μm.

For the estimation of the friction coefficient, the contact force ratio $T(t)/N(t)$ is used for the 10 N excitation case at the corresponding resonance frequency (Fig. 12b). The 10 N excitation case is deliberately chosen because it represents the largest excitation amplitude, bringing the dampers closest to the gross slip condition. For a damper during gross

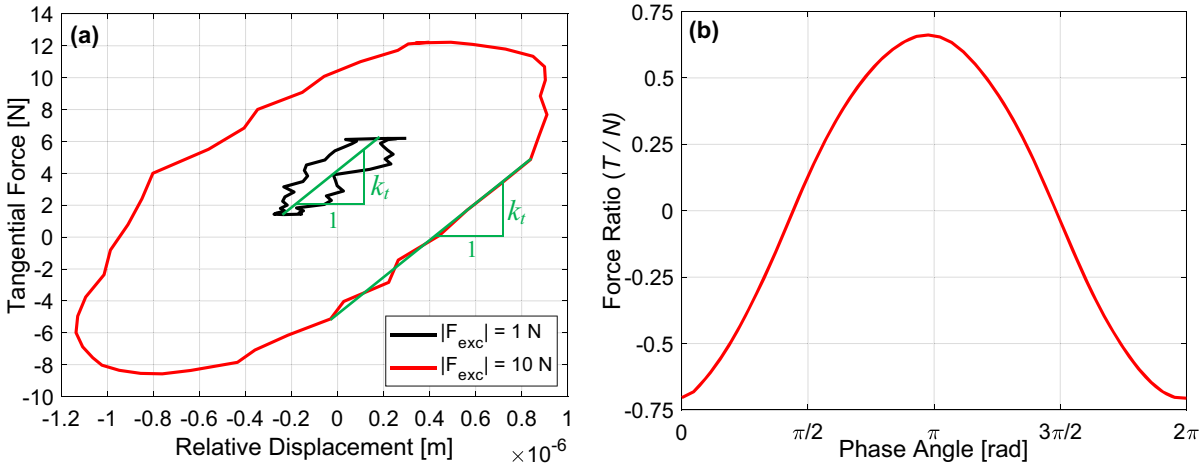

Fig. 12 Measured hysteresis curves and contact force ratio

slip, the contact force ratio, $T(t)/N(t)$, is expected to be equal to the friction coefficient μ, however, in our experiments, gross slip is never achieved, as indicated by the fact that the ratio does not remain constant over one full vibration cycle (Fig. 12b). Nevertheless, the maximum value of the curve provides an insight on a lower reference, which is approximately 0.6. Consequently, the actual value of coefficient of friction is considered to be greater than this estimated reference value due to the absence of gross slip in the experiments.

4.2 Calibration of the linear model

The calibration of the linear model consists of two main steps. First, model updating is performed for the stand-alone blade by correlating experimental and computational results of the natural frequency. In the second step, linear model is calibrated considering linear responses of both free and fully stuck cases. Overview of the linear model calibration process is depicted in Fig. 13.

In the first step, a close match is aimed between the numerically predicted natural frequency and the experimentally measured value of 122.25 Hz. To explore the sensitivity of the results, ten different linear models are constructed, considering three specific parameters. These parameters are as follows:

1. Finite element type: Two different 3D finite elements are employed. The first type is a low-order element with eight nodes in a single element, while the second type is a higher-order element with twenty nodes.
2. Mesh density: The density refers to the number of elements that span through the thickness of the blade. Five different mesh densities are considered. For example, if the blade thickness is divided into two elements, it is referred to as a *2 Elements model*. Consequently, a higher number of elements corresponds to a more intense mesh density.
3. Boundary conditions: Two distinct configurations are created based on the boundary conditions at the root of the model. In the first configuration, the root is fully clamped, applying constraints to all its nodes. In the second configuration, the constraints are only applied to a subset of clamping nodes, selected arbitrarily but uniformly. Hence, the second configuration has a reduced number of clamped nodes and is referred to as the *relaxed configuration*.

Table 1 presents the iterations based on the modal analysis results obtained from the 10 considered models. The first four models utilize the low-order element type with different mesh densities and clamping conditions. However, these models do not yield satisfactory results, as the error remains around 7%, which is high for linear simulations. Additionally, the results show almost no sensitivity to the clamping conditions. In the fifth model, the element type is changed to the high-order element type, leading to a significant improvement as the results overlap accurately. This highlights the necessity of using a higher-

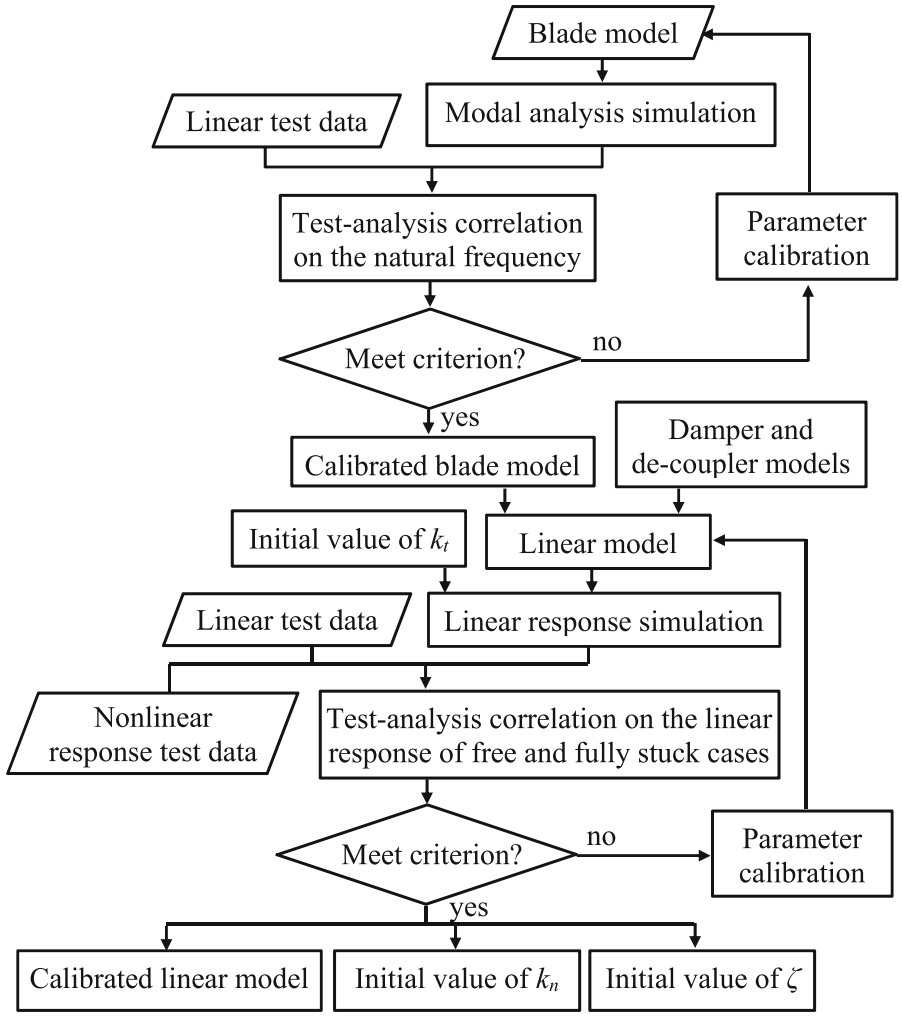

Fig. 13 Overview of the calibration process of the linear model

Table 1 Computational modal analysis results for different stand-alone blade models

Model number	Element type	Mesh density	Boundary condition	Natural freq. [Hz]	Error (%)
1	Low order	3 Elements	Full	137.1	12.2
2	Low order	3 Elements	Relaxed	137.0	12.1
3	Low order	4 Elements	Full	131.1	7.2
4	Low order	4 Elements	Relaxed	131.0	7.1
5	High order	4 Elements	Full	122.1	0.12
6	High order	5 Elements	Full	122.1	0.12
7	High order	2 Elements	Full	122.4	0.12
8	High order	2 Elements	Relaxed	121.9	0.29
9	High order	1 Element	Full	122.6	0.29
10	High order	1 Element	Relaxed	122.1	0.12

order element type for achieving an accurate model. Subsequently, the sixth model investigates the impact of increasing mesh density. The analysis reveals that the natural frequency has already reached a saturation point, indicating no further improvement in model accuracy. Additional models (7–10) were also constructed for further investigation, but no substantial enhancement is observed. This highlights the strong dependence of modal analysis results on the finite element type employed in the model. Based on these findings, the sixth model, depicted in Fig. 8, is selected for the blade in the subsequent analyses.

The second step is to achieve a close alignment between the numerically predicted linear response curves and their experimentally measured counterparts. Both free (stand-alone blade) and fully stuck (coupled blade-damper-decoupler) configurations are considered. In the numerical simulations of fully stuck configuration, the dampers are coupled to the blade and de-couplers using linear springs with tangential and normal contact stiffness values. The experimental results for this configuration consider one arbitrary response curve with the lowest forcing level (1 N), although this scenario does not precisely represent the fully stuck linear configuration due to slight dissipation in it (see Fig. 12a). Since no measurements were taken with lower excitations, this case is utilized for demonstrative purposes. Nevertheless, despite its limitation, this correlation provides initial insights into the contact stiffness parameters through a qualitative comparison on the response curves. The final values will be tuned during subsequent iterations of the nonlinear model calibration.

To investigate the sensitivity of the results, three iterations are performed, taking into account four parameters:

1. Tangential contact stiffness, k_t: The initial estimate of k_t was given in Sect. 4.1 based on the nonlinear test data. This parameter is also considered here and further calibrated with the fully stuck linear configuration.
2. Normal contact stiffness, k_n: A direct measurement of k_n is not available in the tests. Its initial value is estimated based on the matching accuracy of the resonance frequency of fully stuck linear response curve between tests and simulations.
3. Damping ratio of the linear model (coupled blade-damper-decoupler), ζ: Rayleigh damping is specified such that ζ is proportional to the first lowest frequency mode of the fully stuck linear system. The calibrated damping ratio will provide an upper reference value, since a slight dissipation is present in the reference test result.
4. Boundary conditions (BC): This parameter was taken into account when tuning the natural frequency of the stand-alone blade and is further calibrated here, also considering the matching accuracy of the response curves. In the relaxed configuration, the constraints are manually applied by grounding the model from the clamping nodes using linear springs with adjustable stiffness values (with approximately two orders of magnitudes higher values of contact stiffness used in the coupled blade-damper-decoupler configuration).

Table 2 and Fig. 14 present the values of parameters utilized in the iterations and the corresponding linear response curves, respectively. In the first iteration, the resonance frequencies of the experimental and computational curves exhibit close proximity, but a notable difference is observed in the lower portion of the resonance region for both free and fully stuck linear configurations. The response curves measured in tests have a wider width compared to the computationally predicted curves. To address this disparity, the clamping condition is relaxed, and other parameters are heuristically adjusted in the second iteration. Consequently, the lower width of the experimental and computational curves becomes almost equal, but the resonance frequency of the stand-alone blade is shifted to the left. This shift is relevant because the root is no longer fully clamped, and a slight elasticity is introduced through springs. The resonance frequency error of the stand-alone blade is around 2.5%, which cannot be considered negligible.

Table 2 Parameters used in the iterations

Iteration	k_t [N/μm]	k_n [N/μm]	ζ (%)	BC	Meet criterion?	
					Free	Stuck
1	8	8	0.2	Full	No	No
2	6.16	6.16	0.35	Relaxed	No	Yes
3	4.65	6.75	0.33	Relaxed	Yes	Yes

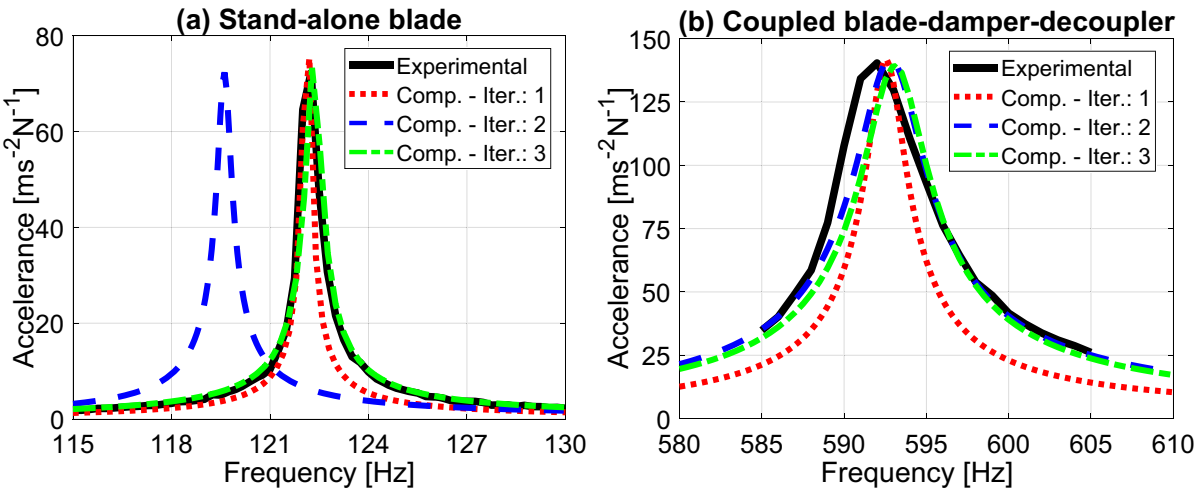

Fig. 14 Comparison of experimental and computational linear response curves for three iterations: **a** free configuration, **b** fully stuck configuration

Additionally, in order to explore the effects of neglected contributions from the sensor mass and shaker stinger on blade dynamics, a lumped mass (for the sensor) and linear springs (for the shaker stinger) are implemented accordingly. Despite an increase in resonance frequency, no further enhancement in accuracy of the linear responses is observed. The outcomes of this iteration indicate that the computational linear response obtained in the second iteration should be shifted to higher frequencies as a whole. In the third iteration, the density of the blade is slightly decreased, and the parameters are further tuned. The matching accuracy of the results can now be considered acceptable, as depicted in Fig. 14 for the third iteration. The assigned density is slightly lower than the actual nominal value of steel, which can be justified by the fact that the manufactured geometry of the blade may not perfectly align with the numerical model due to geometric tolerances. It is important to emphasize that all the calibrations conducted thus far serve to provide initial insights into the parameters that will be used in the calibration of the nonlinear model. The actual values will be tuned considering the sensitivity of uncertainty bands associated with nonlinear response and contact forces.

4.3 Calibration of the nonlinear model

In the nonlinear model calibration process, three parameters are treated as uncertain:

1. Initial position of slip displacements of permanently sticking contacts, $w(t_{\text{ini}})$, hence the initial value of static tangential forces, $T(t_{\text{ini}})$. This uncertainty arises due to different loading histories and is directly addressed in the optimization algorithm that considers and solves also for the unknown multiplier coefficients, m, during the computation of response limits.
2. Contact parameters, i.e., k_t, k_n and μ. The uncertainty in these parameters stems from the limited knowledge about their exact values during the tests. The initial estimates are considered based on the test data and linear model calibration. In each iteration of the nonlinear model calibration process, these parameters are assigned a specific single value. The model is then iteratively calibrated to determine whether the experimental and simulation results better align, taking into account the sensitivity of the response limits to these parameters.
3. The alignment of the test setup, particularly the dampers and pre-loads. This uncertainty arises due to the lack of precise information regarding the system's symmetry and the positioning of the dampers. Initially, the configuration of the model is taken into account with a perfect symmetry. In each iteration, a particular configuration is considered, and this configuration is calibrated based on the sensitivity of contact force limits to the test alignment.

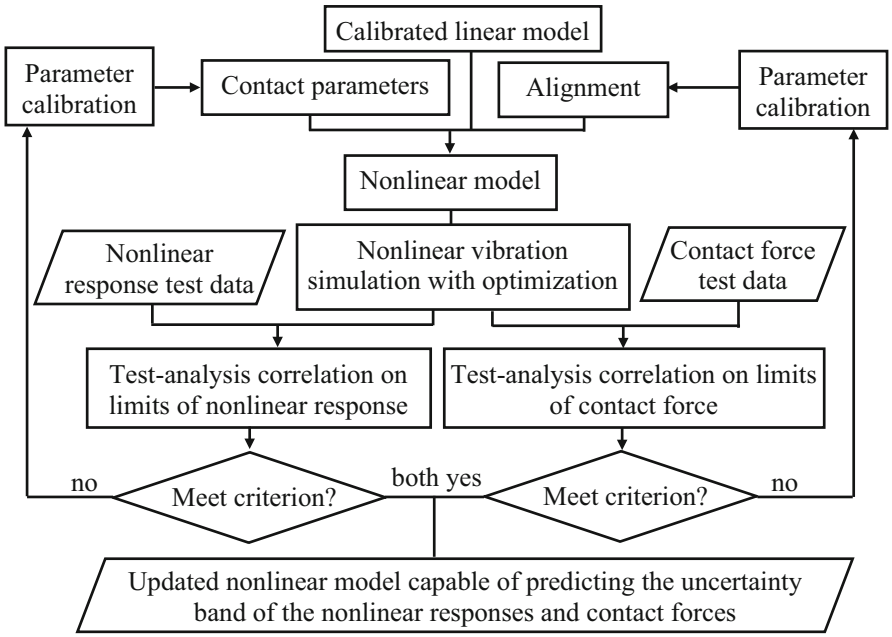

Fig. 15 Overview of the calibration process of the nonlinear model

Based on these three sources of uncertainty, the response variability in numerical simulations is achieved by the forward propagation of only the first uncertainty into the nonlinear dynamics of the structure. The parameters associated to the second and the third uncertainties are treated as having a single specific value and configuration in each iteration of the calibration process. An overview of the nonlinear model calibration is shown in Fig. 15.

The calibration process consists of four iterations. It is important to underline that this process is not straightforward, as it entails addressing multiple uncertainties associated with several parameters that need to be considered concurrently. The objective here is to achieve a satisfactory level of accuracy in predicting the limits of both the multiple nonlinear responses and contact forces. The values of the contact parameters and the model alignment configuration are summarized in Fig. 16. The linear damping ratio, ζ, is set to 0.2% in all iterations. The initial parameters for the first iteration are consistently selected with the findings from the earlier sections on linear model calibration (Sect. 4.2) and nonlinear test data (Sect. 4.1).

4.3.1 Iteration 1

This iteration serves as an initial attempt to gain a general understanding of the overall results. The alignment is considered with a perfect symmetry. Figure 17a–d presents the test results of the multiple nonlinear responses and the predicted limits obtained through optimization for four different excitation levels. The upper limits align closely with the resonance regime of the experimental curves, while the lower limits exhibit a pronounced softening behavior. Further, the resonance frequency of the lower limits shift toward smaller values as the excitation level increases. To comprehend the main cause of this phenomenon, the contact states of the lower limits at the resonance frequencies are investigated. It is observed that while many contact points alternate between stick–slip states, full separation occurs at certain contact points. This implies that the optimization algorithm converges to a particular contact configuration where some contact nodes are fully separated, resulting in the system's loss factor reaching its maximum value for the computation of lower limit. The number of points undergoing full separation increases with larger excitations, leading to higher stiffness loss for the lower limit. Conversely, the surfaces remain in contact for the upper limits, with no damping present even in cases with 1 N and 3 N excitations. The optimization simulations provide the theoretical limits that the experimental curves can reach, successfully capturing the variability range of the test data in terms of amplitudes. However, the

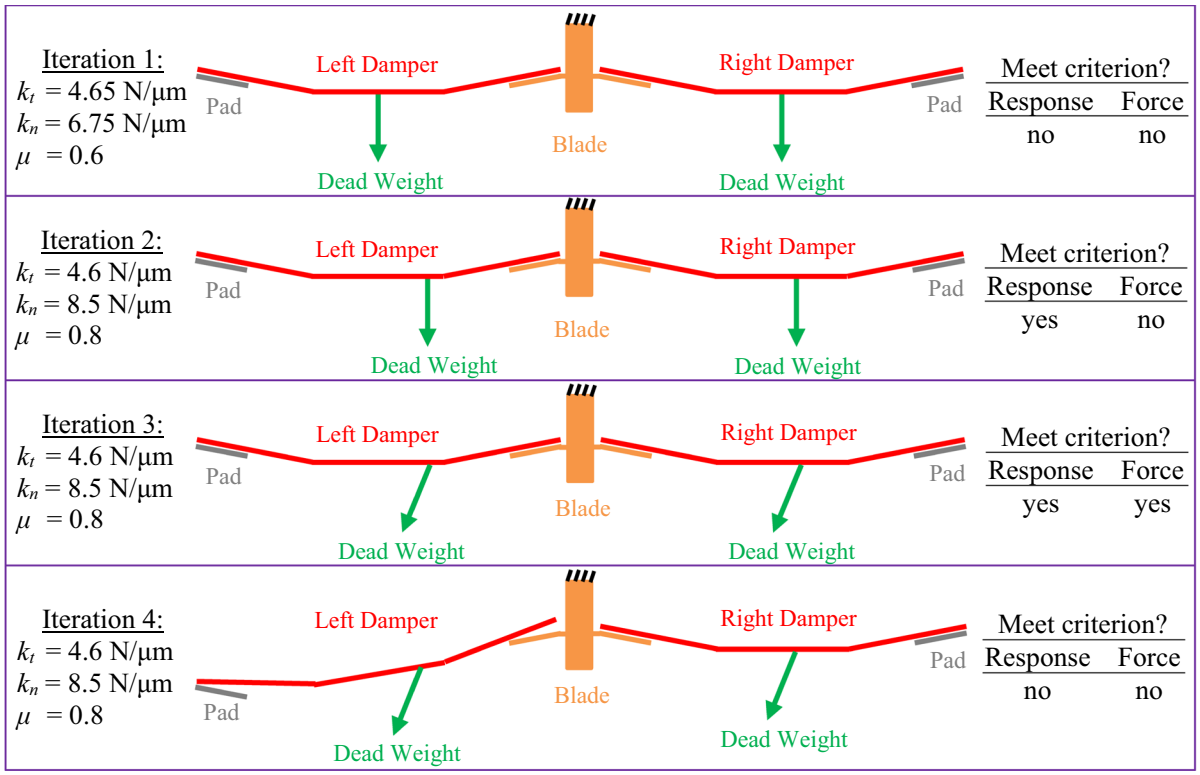

Fig. 16 The value of contact parameters and schematic sketch of the model alignment for different iterations

resonance frequency of the upper limit could be slightly shifted to a higher frequency by further tuning of the contact parameters.

In addition to capturing the response variability, the optimization algorithm determines the limits of static tangential contact forces. Figure 18 depicts the measured multiple contact forces and the predicted limits from the first iteration for the 10 N excitation case. The dynamic components of the upper limit closely match the experimental data, while those of the lower limit are noticeably smaller. This is relevant because the response curve of the upper limit for $|F_{exc}|$= 10 N (see Fig. 17d) closely resembles the experimental curves, indicating that the contact forces are expected to be similar as well. Figure 18 demonstrates that the predicted limits of tangential static forces effectively capture the range of variability observed in the test results, indicating the correct functioning of the optimization algorithm. However, as also mentioned in Sect. 2.3.2, there exists a disparity in the measured static normal force values between the left and right dampers, indicating a misalignment in the assembly. The predicted limits and measured results of static normal forces on the left damper show significant discrepancies, indicating that the symmetric configuration does not accurately reflect the actual scenario. The results for other excitation levels follow a similar pattern, but they are not presented here for the sake of brevity. To address the difference in normal forces and account for the misalignment, the pre-loads on the dampers are adjusted accordingly in the next iteration.

4.3.2 Iteration 2

The contact parameters are heuristically tuned to achieve a slight upward shift in the resonance frequency of the upper limits, while still ensuring that the predicted limits effectively capture the measured range of response variability. Through fine calibration, it is found that among the three contact parameters, k_t exhibits greater sensitivity in influencing the behavior of the limits. Therefore, k_t is slightly modified, while k_n and μ are set to relatively higher values (refer to the final values in Fig. 16).

Additionally, the position of the dead weights on the dampers is altered to mimic the misalignment

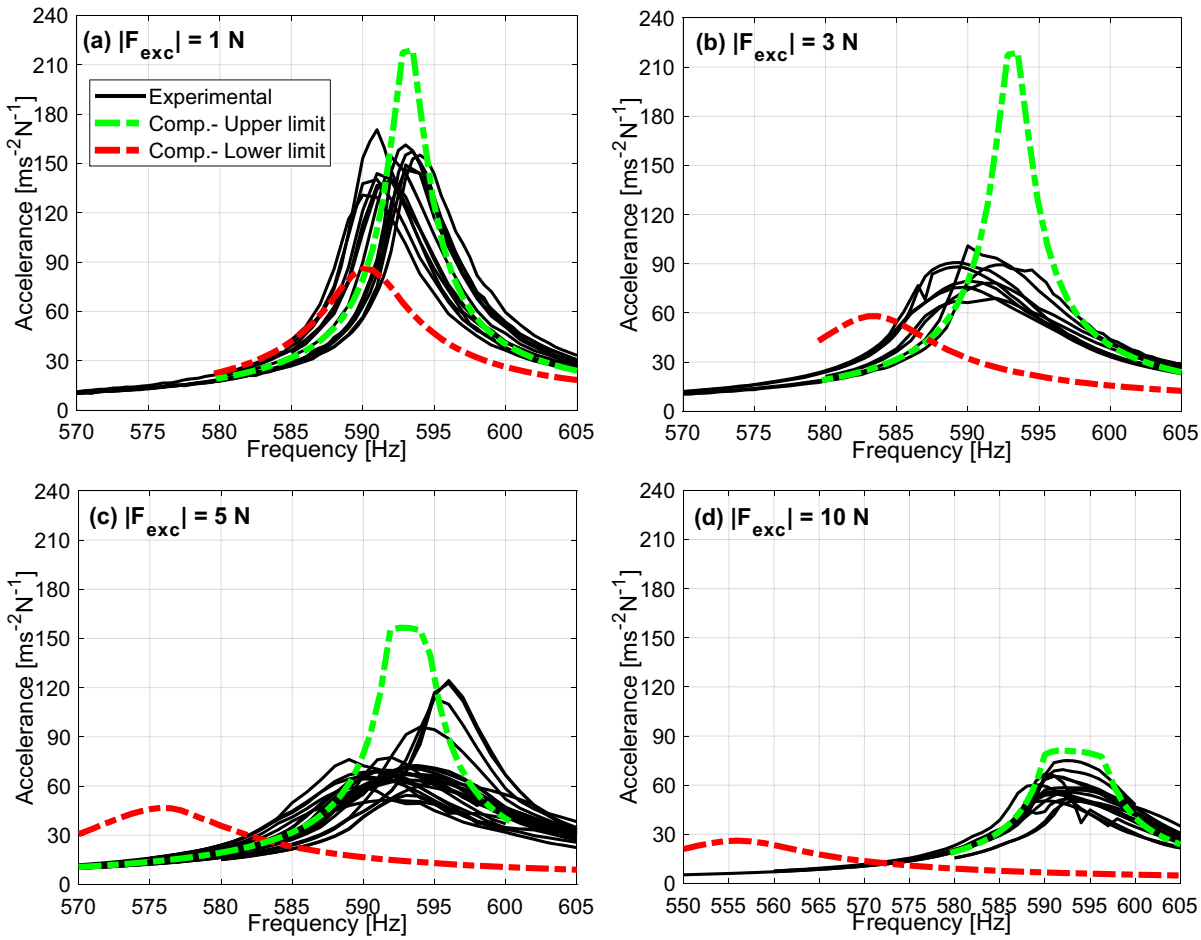

Fig. 17 Measured multiple nonlinear responses and predicted limits for the 1st iteration

Fig. 18 Measured multiple contact forces and predicted limits for the 1st iteration ($|F_{exc}|$= 10 N)

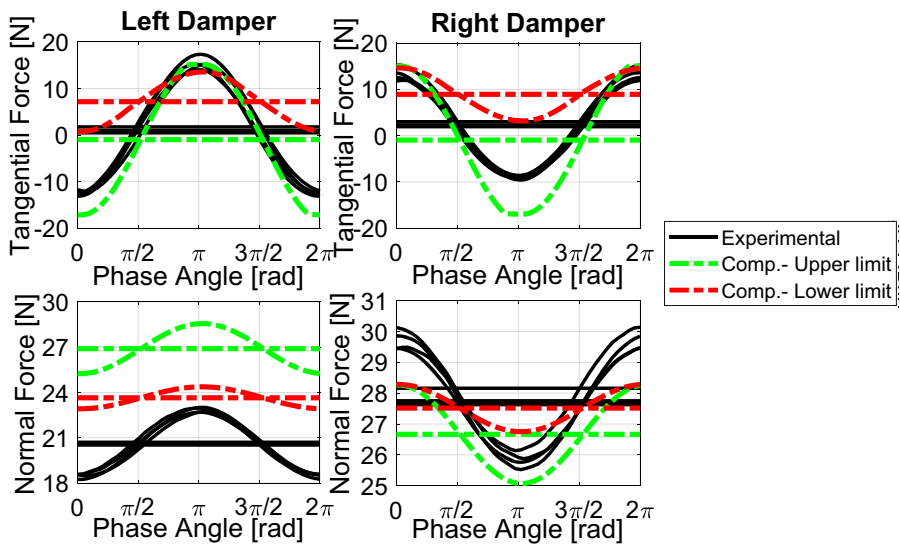

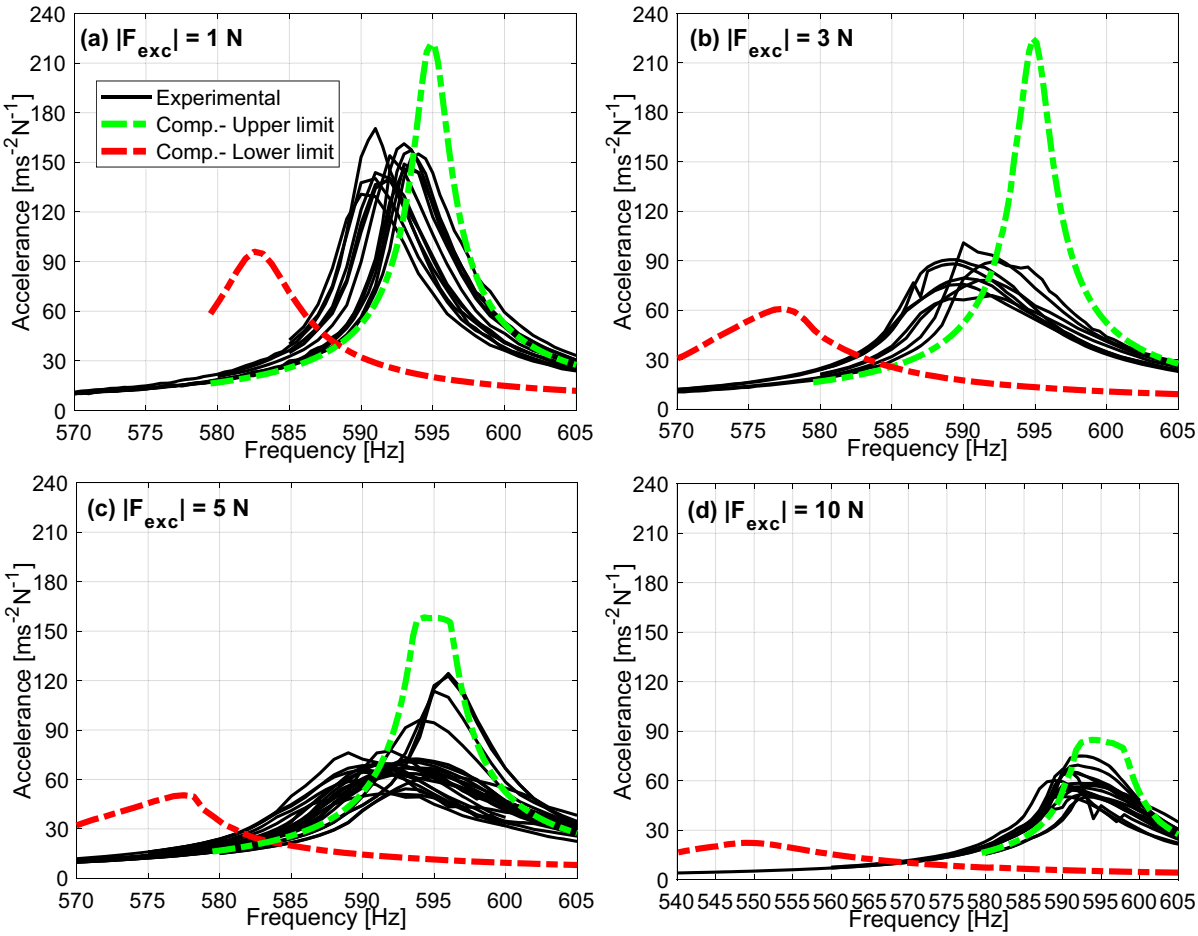

Fig. 19 Measured multiple nonlinear responses and predicted limits for the 2nd iteration

present in the actual system. This calibration is performed based on the deviation ratio between the test and simulation results of normal contact forces. First, the ratio between the average values of the normal static components of the upper and lower limits and those obtained using the test data (Fig. 18) are calculated. Subsequently, the pre-load on the dampers is shifted by proportioning this ratio to the horizontal length of the damper, either toward the blade side or the decoupler side. For instance, as the ratio is approximately 20% $((25.5 - 21)/21 \times 100)$ for the left damper, the preload is shifted toward the blade side by 20% of the horizontal length of the damper to reduce the normal force values of predicted limits. Analogously, for the right damper, the preload is slightly shifted toward the decoupler side to increase the limit values of the static components. Note that the contact forces given in Fig. 18 are for the de-coupler side of the dampers. Simplified schematic of the alignment of the pre-loads are shown in Fig. 16.

Figure 19 shows the measured multiple nonlinear response and the predicted limits. The trend of the limits for different excitation levels remains similar to the previous iteration, effectively capturing the range of variability with acceptable accuracy. This outcome indicates that changing the position of the pre-loads does not significantly impact the response behavior; instead, its influence is more prominent on the contact forces, as depicted in Fig. 20, particularly on the normal contact forces. More specifically, for 10 N excitation case in Fig. 20a, the computed normal force curves corresponding to the upper limit closely align with the test data. The deviation between the normal static components of the test data and limits is also compensated on both dampers. Further, the variability range of the static tangential forces is effectively

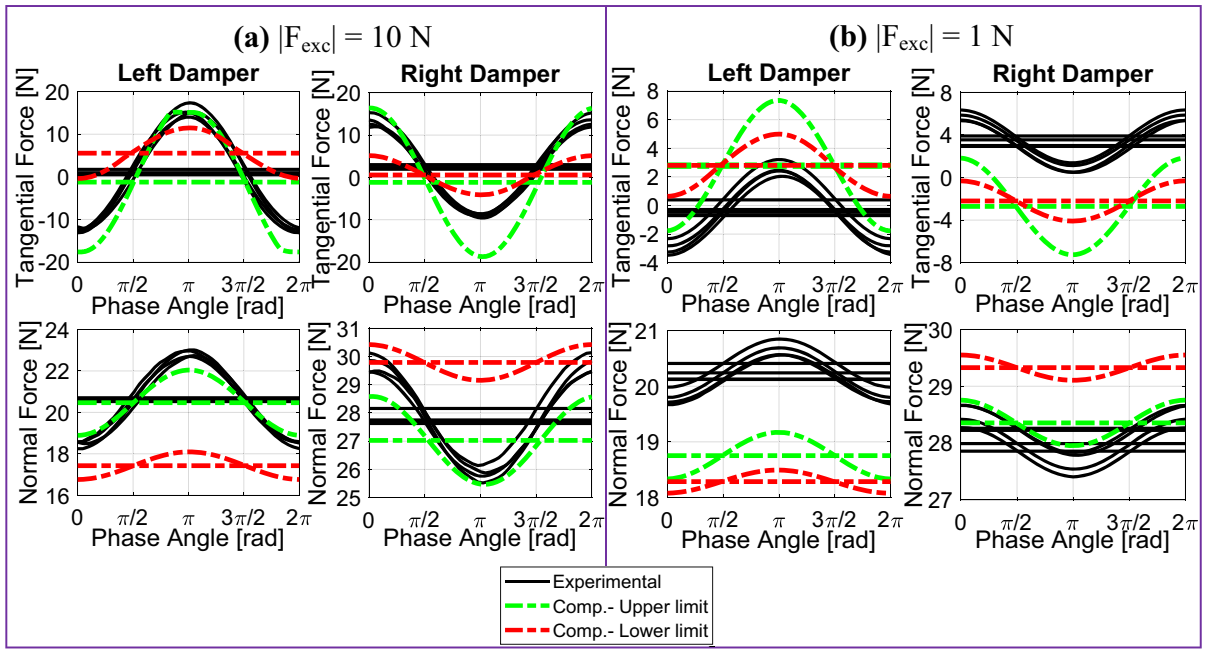

Fig. 20 Measured multiple contact forces and predicted limits for the 2nd iteration

captured on the left damper, while there is a slight discrepancy for the right damper. To compare the contact forces obtained also with other excitation amplitudes, Fig. 20b presents the results for the 1 N forcing level. The results for this case are not as satisfactory as those for the 10 N case. The static components of the computational results deviate significantly from their experimental counterparts, which cannot be considered negligible. This implies that further tuning, particularly regarding the alignment of the pre-loads, is necessary to enhance the matching accuracy between the computed and experimental results.

4.3.3 Iteration 3

The contact parameters that provided accurate results in the previous iteration are retained with the same values for this iteration. The focus in this iteration is on adjusting the pre-loads on the dampers to better represent the misalignment in the model, particularly introducing an inclination angle on the application of the pre-loads. The inclination angles for the pre-loads are determined through a heuristically performed sensitivity analysis, which involves performing several analyses with different inclination angles. The objective is to achieve the highest possible matching accuracy for all excitation cases. Based on the sensitivity analysis, the inclination angles are set to 3 degrees for the left damper and 5 degrees for the right damper, both inclined toward the left side (see Fig. 16). The position of the pre-loads remains the same as in the previous iteration.

The optimization algorithm successfully computes the variability in the measured nonlinear response, as depicted in Fig. 21. This shows that contact parameters have been accurately calibrated. The results of the contact forces for all excitation levels are presented in Fig. 22. The key observations from the results are as follows:

1. The dynamic components of the contact forces and their amplitudes exhibit good consistency between the experimental tests and simulations for all excitation levels.
2. The predicted limits of the multiple static tangential forces align accurately with the experimental data. Although small deviations are still present, they can be considered negligible, as the overall agreement between the experimental and computational results is coherent. This demonstrates that the optimization algorithm successfully predicts not only the limits of the nonlinear response but

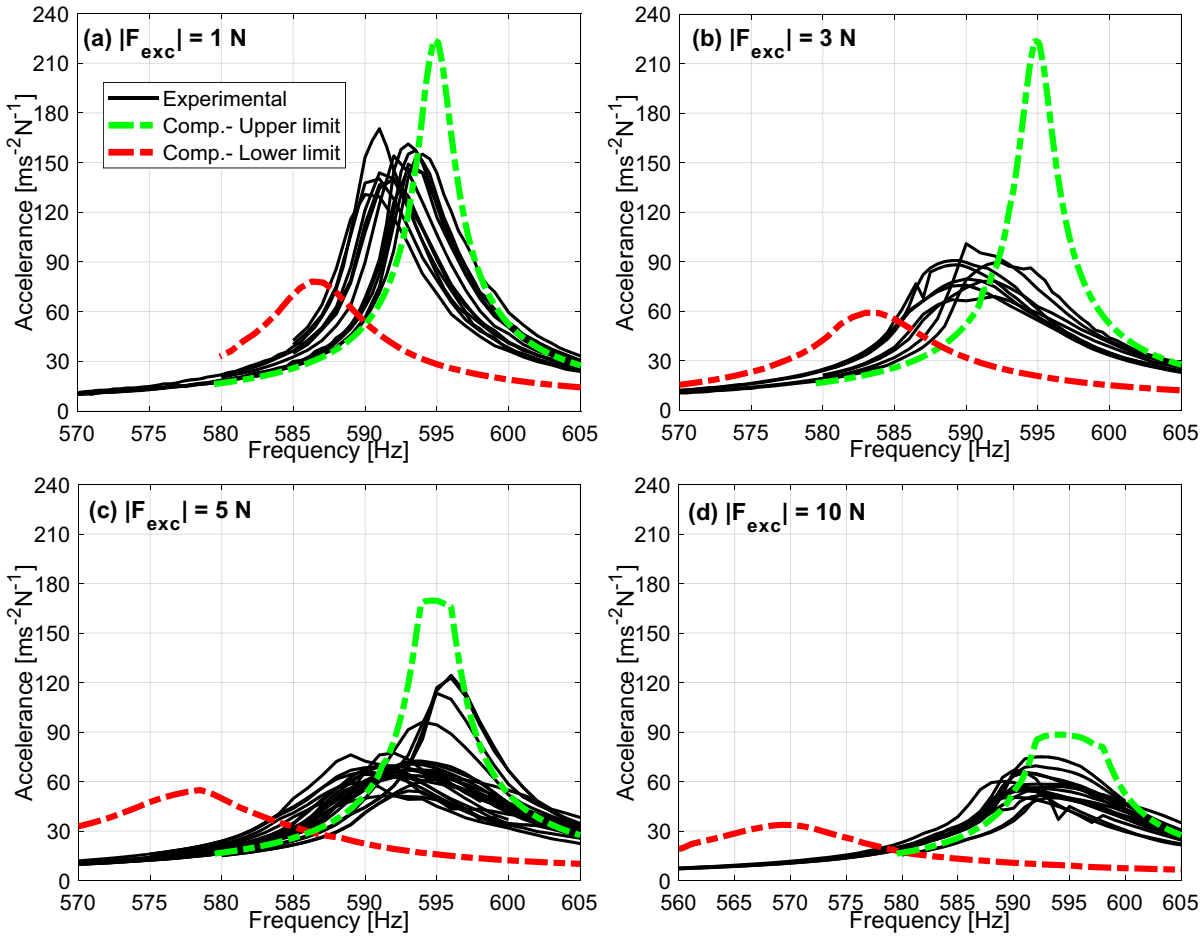

Fig. 21 Measured multiple nonlinear responses and predicted limits for the 3rd iteration

also the limits of the static tangential forces, which was the main objective of the calibration process.

3. Some unavoidable discrepancies are observed in the static components of the normal forces between the tests and simulations. The largest deviation, approximately 7%, is observed on the left damper for the 5 N excitation case (see Fig. 22c). It is important to note that the presented model updating procedure simultaneously considers the results of 20 different cases (16 for contact forces and 4 for responses) by employing multiple parameters to achieve maximum agreement between predictions and tests for a complex structure. Therefore, it is natural to expect slight deviations in certain results, while the overall results can be considered satisfactory in terms of accuracy, particularly when considering the predicted limits of the measured multiple nonlinear response and static tangential contact forces.

Consequently, based on the results of this iteration, it can be inferred that the comprehensive model calibration can be deemed successful using the selected contact parameters and alignment configuration of the test assembly.

4.3.4 Iteration 4

To further improve the matching accuracy of the normal contact forces, an additional iteration is carried out, despite the satisfactory results obtained in the previous iteration. In this iteration, the left damper is rotated, as illustrated in an exaggerated manner in Fig. 16. The rotation is modeled by introducing initial

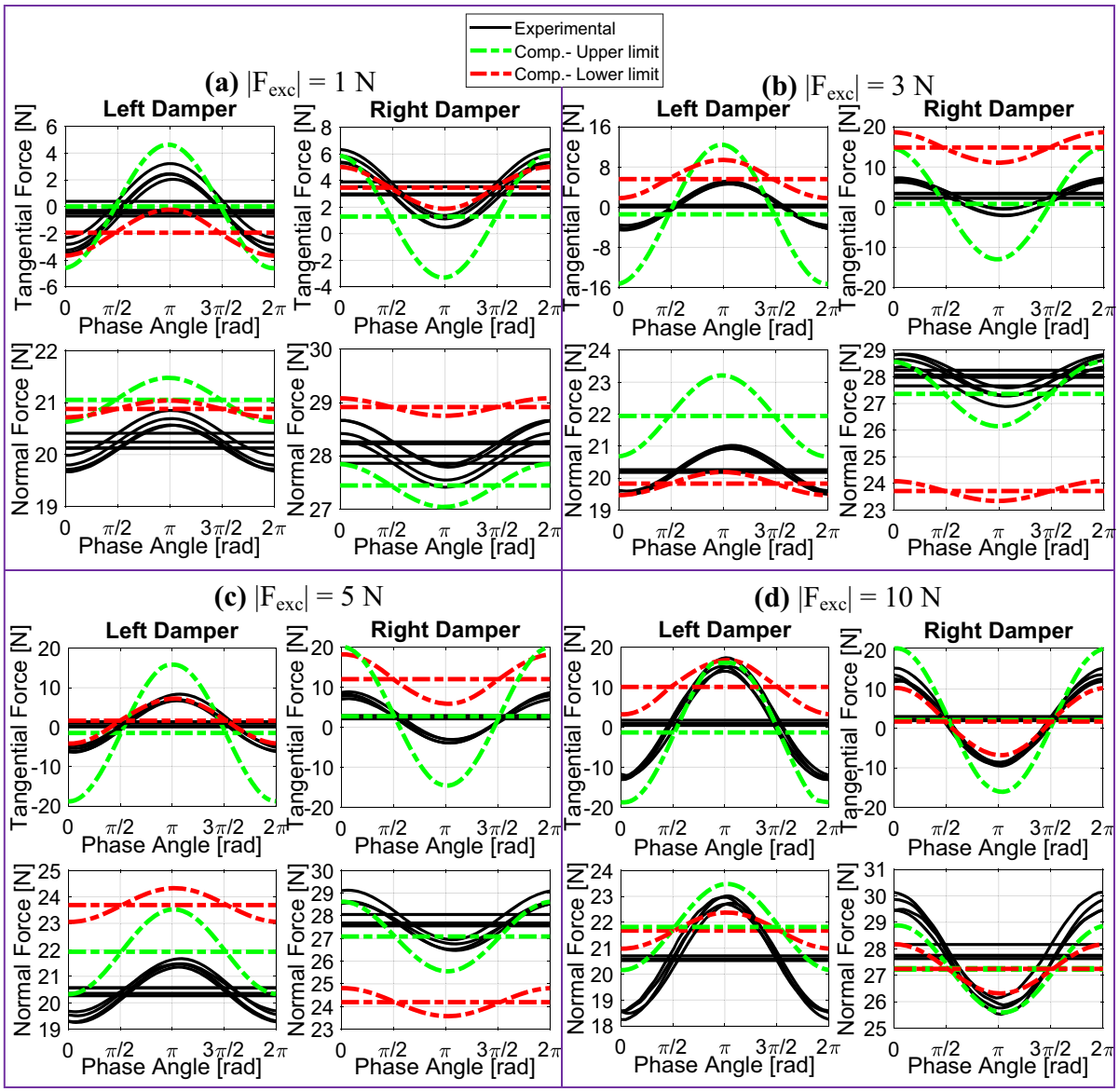

Fig. 22 Measured multiple contact forces and predicted limits for the 3rd iteration

gaps into the contact elements. These gaps are distributed proportionally along the contact line with linearly increasing values. By introducing this rotation and modeling the corresponding initial gaps, the aim is to achieve a more accurate representation of the misalignment in the model and consequently improve the matching accuracy of the normal contact forces. A sensitivity analysis is conducted to explore the impact of various rotation angles on the results in separate analyses. For demonstration, the case with a rotation angle of 0.35 degrees is presented here. It should be noted that the contact parameters remain unchanged from the previous iteration.

In this iteration, as depicted in Fig. 23, there is a noticeable difference in the resonance frequencies of the limits compared to the experimental data. Unlike the previous three iterations, the resonance frequencies of the limits, including the upper limit, are considerably lower than their experimental counterparts. Only for the 10 N excitation case, the resonance frequency remains similar to the previous iterations. The shift in frequencies is attributed to the occurrence

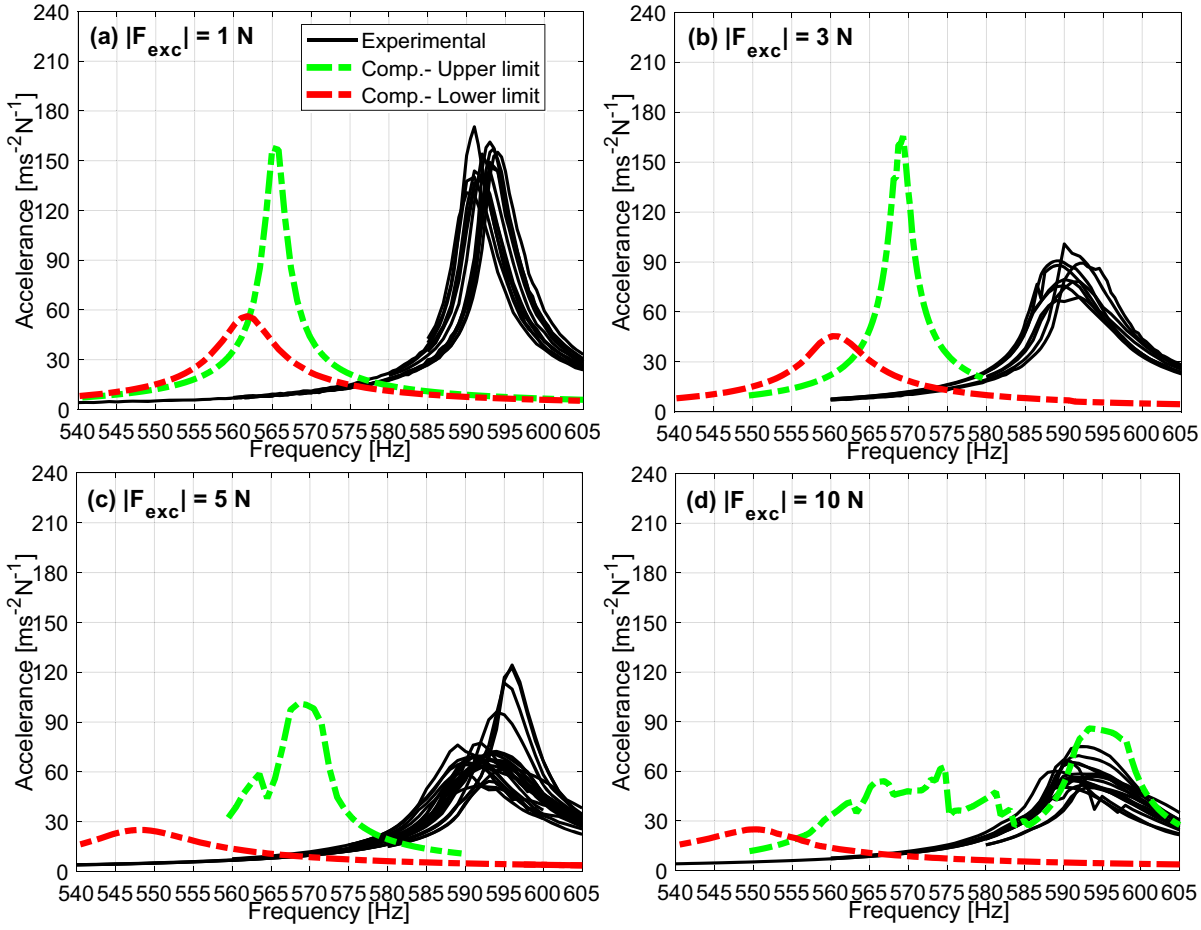

Fig. 23 Measured multiple nonlinear response and predicted limits for the 4th iteration

of full separation at some contact nodes. The initial gaps introduced due to the rotation of the left damper remain open at low vibration levels at small excitation cases, leading to full separation at certain contact points. As the forcing levels increase, more mating points come into contact, resulting in a shift of the resonance frequency of the upper limit curve to higher values, as observed from Fig. 23a to Fig. 23d. Further, as the nonlinearity level increases due to the stick–slip-separation phenomenon at higher excitations, the optimization algorithm faces challenges in finding the minimum value of the loss factor. This results in a jumping behavior of the upper limit curves, as shown in Fig. 23c and 23d. It is important to note that the algorithm converges even for jumping responses, however the obtained value of the loss factor may not represent the global minimum. Since the nonlinear responses do not already match well in this iteration, the contact forces are not provided as part of the analysis.

In summary, after an extensive calibration process involving multiple iterations with several parameters, the third iteration resulted in the highest level of agreement between the experimental tests and the computational simulations. The specific values of the contact parameters and the alignment configuration used in the third iteration were presented in Fig. 16, reflecting the culmination of the calibration efforts to achieve an accurate representation of the system's behavior.

5 Summary and conclusion

This study presents a deterministic model calibration process using multiple test data of a friction-damped

turbine blade coupled with mid-span dampers. An optimization algorithm is employed to predict the limits of the measured multiple nonlinear response and contact forces. This algorithm specifically addresses the epistemic uncertainty associated with the static tangential forces of permanently sticking contacts. The model is iteratively tuned, taking into account the sensitivity of the limits to both contact parameters and the alignment of the test setup. The adoption of this non-probabilistic approach constitutes a novel contribution to the field, because the challenges associated with model updating procedures for friction-damped turbine blades with multiple test data are typically addressed using statistical and stochastic techniques in the community.

The main findings and interpretations of the current study can be summarized as follows:

- The limits of the variability in the nonlinear response are primarily influenced by the contact parameters, except when an initial gap is introduced in the contact elements.
- The variability limits of the contact forces are mainly affected by the alignment of the damper's positioning and the application of preload.
- Despite small discrepancies observed in a few cases, the overall accuracy of the results can be considered satisfactory.
- The optimization algorithm effectively addresses the uncertainty associated with the static tangential forces in permanently sticking contacts.
- The calibration of the linear model is crucial for gaining initial insights into the values of tangential and normal contact stiffness.

This study sheds light on various practical aspects involved in the process of matching computational and experimental results through several iterations of the model. As a result, it provides a framework for designers engaged in the calibration procedures of frictional turbine blade models with multiple test data.

Funding Open access funding provided by Politecnico di Torino within the CRUI-CARE Agreement.

Data availability Data will be made available on reasonable request.

Declarations

Conflict of interest The authors declare that they have no known competing financial interests or personal relationships that could have appeared to influence the work reported in this paper.

References

1. Griffin, J.H.: Friction damping of resonant stresses in gas turbine engine airfoils. J. Eng. Power **102**(2), 329–333 (1980). https://doi.org/10.1115/1.3230256
2. Cowles, B.A.: High cycle fatigue in aircraft gas turbines—an industry prospective. Int. J. Fract. **80**(2–3), 147–163 (1996). https://doi.org/10.1007/BF00012667
3. Srinivasan, A.V.: Flutter and resonant vibration characteristics of engine blades. ASME J. Eng. Gas Turbines Power **119**(4), 742–775 (1997). https://doi.org/10.1115/1.2817053
4. Krack, M., Salles, L., Thouverez, F.: Vibration prediction of bladed disks coupled by friction joints. Arch. Comput. Methods Eng. **24**(3), 589–636 (2017). https://doi.org/10.1007/s11831-016-9183-2
5. Gaul, L., Lenz, J.: Nonlinear dynamics of structures assembled by bolted joints. Acta Mech. **125**(1), 169–181 (1997). https://doi.org/10.1007/BF01177306
6. Hartwigsen, C.J., Song, Y., McFarland, D.M., Bergman, L.A., Vakakis, A.F.: Experimental study of non-linear effects in a typical shear lap joint configuration. J. Sound Vib. **277**(1–2), 327–351 (2004). https://doi.org/10.1016/j.jsv.2003.09.018
7. Roettgen, D.R., Allen, M.S.: Nonlinear characterization of a bolted, industrial structure using a modal framework. Mech. Syst. Signal Process. **84**, 152–170 (2017). https://doi.org/10.1016/j.ymssp.2015.11.010
8. Brake, M.R.W., Schwingshackl, C.W., Reuß, P.: Observations of variability and repeatability in jointed structures. Mech. Syst. Signal Process. **129**, 282–307 (2019). https://doi.org/10.1016/j.ymssp.2019.04.020
9. Krack, M., Panning, L., Wallaschek, J., Siewert, C., Hartung, A.: Robust design of friction interfaces of bladed disks with respect to parameter uncertainties. In: *Turbo Expo: Power for Land, Sea, and Air*. American Society of

Mechanical Engineers, Vol. 44731, pp. 1193–1204 (2012). https://doi.org/10.1115/GT2012-68578.
10. Petrov, E.P.: Analysis of sensitivity and robustness of forced response for nonlinear dynamic structures. Mech. Syst. Signal Process. **23**(1), 68–86 (2009). https://doi.org/10.1016/j.ymssp.2008.03.008
11. Sanliturk, K.Y., Ewins, D.J., Stanbridge, A.B.: Underplatform dampers for turbine blades: theoretical modeling, analysis and comparison with experimental data. ASME J. Eng. Gas Turbines Power **123**(4), 919–929 (2001). https://doi.org/10.1115/1.1385830
12. Sever, I.A., Petrov, E.P., Ewins, D.J.: Experimental and numerical investigation of rotating bladed disk forced response using underplatform friction dampers. ASME J. Eng. Gas Turbines Power **130**(4), 042503 (2008). https://doi.org/10.1115/1.2903845
13. Schwingshackl, C.W., Petrov, E.P., Ewins, D.J.: Measured and estimated friction interface parameters in a nonlinear dynamic analysis. Mech. Syst. Signal Process. **28**, 574–584 (2012). https://doi.org/10.1016/j.ymssp.2011.10.005
14. Gastaldi, C., Gola, M.M.: On the relevance of a microslip contact model for under-platform dampers. Int. J. Mech. Sciences **115–116**, 145–156 (2016). https://doi.org/10.1016/j.ijmecsci.2016.06.015
15. Pesaresi, L., Salles, L., Jones, A., Green, J.S., Schwingshackl, C.W.: Modelling the nonlinear behaviour of an underplatform damper test rig for turbine applications. Mech. Syst. Signal Process. **85**, 662–679 (2017). https://doi.org/10.1016/j.ymssp.2016.09.007
16. Lacayo, R., Pesaresi, L., Groß, J., Fochler, D., Armand, J., Salles, L., Schwingshackl, C., Allen, M., Brake, M.: Nonlinear modeling of structures with bolted joints: a comparison of two approaches based on a time-domain and frequency-domain solver. Mech. Syst. Signal Process. **114**, 413–438 (2019). https://doi.org/10.1016/j.ymssp.2018.05.033
17. Li, D., Xu, C., Liu, T., Gola, M.M., Wen, L.: A modified IWAN model for micro-slip in the context of dampers for turbine blade dynamics. Mech. Syst. Signal Process. **121**, 14–30 (2019). https://doi.org/10.1016/j.ymssp.2018.11.002
18. Sinou, J.J., Didier, J., Faverjon, B.: Stochastic non-linear response of a flexible rotor with local non-linearities. Int. J. Non-Linear Mech. **74**, 92–99 (2015). https://doi.org/10.1016/j.ijnonlinmec.2015.03.012
19. Panunzio, A.M., Salles, L., Schwingshackl, C.W.: Uncertainty propagation for nonlinear vibrations: a non-intrusive approach. J. Sound Vib. **389**, 309–325 (2017). https://doi.org/10.1016/j.jsv.2016.09.020
20. Sun, Y., Yuan, J., Pesaresi, L., Denimal, E., Salles, L.: Parametric study and uncertainty quantification of the nonlinear modal properties of frictional dampers. J. Vib. Acoust. **142**(5), 051102 (2020). https://doi.org/10.1115/1.4046953
21. Yuan, J., Fantetti, A., Denimal, E., Bhatnagar, S., Pesaresi, L., Schwingshackl, C., Salles, L.: Propagation of friction parameter uncertainties in the nonlinear dynamic response of turbine blades with underplatform dampers. Mech. Syst. Signal Process. **156**, 107673 (2021). https://doi.org/10.1016/j.ymssp.2021.107673
22. Metropolis, N., Ulam, S.: The monte carlo method. J. Am. Stat. Assoc. **44**(247), 335–341 (1949). https://doi.org/10.1080/01621459.1949.10483310
23. Butlin, T.: Anti-optimisation for modelling the vibration of locally nonlinear structures: an exploratory study. J. Sound Vib. **332**(26), 7099–7122 (2013). https://doi.org/10.1016/j.jsv.2013.06.028
24. Butlin, T., Ghaderi, P., Spelman, G., Midgley, W.J.B., Umehara, R.: A novel method for predicting the response variability of friction-damped gas turbine blades. J. Sound Vib. **440**, 372–398 (2019). https://doi.org/10.1016/j.jsv.2018.10.013
25. Butlin, T., Spelman, G., Ghaderi, P., Midgley, W.J.B., Umehara, R.: Predicting response bounds for friction-damped gas turbine blades with uncertain friction coupling. J. Sound Vib. **440**, 399–411 (2019). https://doi.org/10.1016/j.jsv.2018.08.037
26. Mitsopoulou, E.N., Doudoumis, I.N.: A contribution to the analysis of unilateral contact problems with friction. Solid Mech. Arch. **12**(3), 165–186 (1987)
27. Klarbring, A.: Examples of non-uniqueness and non-existence of solutions to quasistatic contact problems with friction. Ing. Arch. **60**(8), 529–541 (1990). https://doi.org/10.1007/BF00541909
28. Barber, J.R., Klarbring, A., Ciavarella, M.: Shakedown in frictional contact problems for the continuum. Comptes Rendus Mécanique **336**(1–2), 34–41 (2008). https://doi.org/10.1016/j.crme.2007.10.013
29. Ponter, A.R.: Shakedown limit theorems for frictional contact on a linear elastic body. Eur. J. Mech. A/Solids **60**, 17–27 (2016). https://doi.org/10.1016/j.euromechsol.2016.05.003
30. Flicek, R.C., Brake, M.R., Hills, D.A., Barber, J.R.: Predicting the shakedown limits of joints subject to fretting and high cycle fatigue. In: The Mechanics of Jointed Structures, pp. 561–582. Springer, Cham (2018). https://doi.org/10.1007/978-3-319-56818-8_31
31. Flicek, R.C., Brake, M.R.W., Hills, D.A.: Predicting a contact's sensitivity to initial conditions using metrics of frictional coupling. Tribol. Int. **108**, 95–110 (2017). https://doi.org/10.1016/j.triboint.2016.09.038
32. Yang, B.D., Menq, C.H.: Characterization of contact kinematics and application to the design of wedge dampers in turbomachinery blading: part 1—stick-slip contact kinematics. J. Eng. Gas Turbines Power **120**(2), 410–417 (1998). https://doi.org/10.1115/1.2818138
33. Yang, B.D., Menq, C.H.: Characterization of contact kinematics and application to the design of wedge dampers in turbomachinery blading: part 2—prediction of forced response and experimental verification. J. Eng. Gas Turbines Power **120**(2), 418–423 (1998). https://doi.org/10.1115/1.2818139
34. Zucca, S., Botto, D., Gola, M.M.: Range of variability in the dynamics of semi-cylindrical friction dampers for turbine blades. In: Proceedings of the ASME Turbo Expo 2008: Power for Land, Sea, and Air. Volume 5: Structures and Dynamics, Parts A and B. Berlin, Germany, pp. 519–529 (2008). https://doi.org/10.1115/GT2008-51058
35. Firrone, C.M., Zucca, S., Gola, M.M.: The effect of underplatform dampers on the forced response of bladed disks by a coupled static/dynamic harmonic balance

method. Int. J. Non-Linear Mech. **46**(2), 363–375 (2011). https://doi.org/10.1016/j.ijnonlinmec.2010.10.001
36. Zucca, S., Firrone, C.M., Gola, M.: Modeling underplatform dampers for turbine blades: a refined approach in the frequency domain. J. Vib. Control **19**(7), 1087–1102 (2013). https://doi.org/10.1177/1077546312440809
37. Zucca, S., Firrone, C.M.: Nonlinear dynamics of mechanical systems with friction contacts: coupled static and dynamic multi-harmonic balance method and multiple solutions. J. Sound Vib. **333**(3), 916–926 (2014). https://doi.org/10.1016/j.jsv.2013.09.032
38. Ferhatoglu, E., Zucca, S., Botto, D., Auciello, J., Arcangeli, L.: Nonlinear vibration analysis of turbine bladed disks with Midspan Dampers. J. Eng. Gas Turbines Power **144**(4), 041021 (2022). https://doi.org/10.1115/1.4053107
39. Gastaldi, C., Gross, J., Scheel, M., Berruti, T.M., Krack, M.: Modeling complex contact conditions and their effect on blade dynamics. J. Eng. Gas Turbines Power **143**(1), 011007 (2021). https://doi.org/10.1115/1.4049186
40. Ferhatoglu, E., Zucca, S.: Determination of periodic response limits among multiple solutions for mechanical systems with wedge dampers. J. Sound Vib. **494**, 115900 (2021). https://doi.org/10.1016/j.jsv.2020.115900
41. Ferhatoglu, E., Groß, J., Krack, M.: Frequency response variability in friction-damped structures due to non-unique residual tractions: obtaining conservative bounds using a nonlinear-mode-based approach. Mech. Syst. Signal Process. **201**, 110651 (2023). https://doi.org/10.1016/j.ymssp.2023.110651
42. Ferhatoglu, E., Zucca, S.: On the non-uniqueness of friction forces and the systematic computation of dynamic response boundaries for turbine bladed disks with contacts. Mech. Syst. Signal Process. **160**, 107917 (2021). https://doi.org/10.1016/j.ymssp.2021.107917
43. Ferhatoglu, E., Gastaldi, C., Botto, D., Zucca, S.: An experimental and computational comparison of the dynamic response variability in a turbine blade with under-platform dampers. Mech. Syst. Signal Process. **172**, 108987 (2022). https://doi.org/10.1016/j.ymssp.2022.108987
44. Ferhatoglu, E., Botto, D., Zucca, S.: An experimental investigation on the dynamic response variability of a turbine blade with mid-span dampers. J. Eng. Gas Turbines Power GTP-22-1373. **145**(1), 011002. https://doi.org/10.1115/1.4055494.
45. Szwedowicz, J., Secall-Wimmel, T., Dünck-Kerst, P.: Damping performance of axial turbine stages with loosely assembled friction bolts: the nonlinear dynamic assessment. J. Eng. Gas Turbines Power (2008). https://doi.org/10.1115/1.2838998
46. Drozdowski, R., Völker, L., Häfele, M., Vogt, D.M.: Experimental and numerical investigation of the nonlinear vibrational behavior of steam turbine last stage blades with friction bolt damping elements. In: Turbo Expo: Power for Land, Sea, and Air, vol. 56796, p. V008T26A007. American Society of Mechanical Engineers (2015). https://doi.org/10.1115/GT2015-42244.
47. Craig JR, R.R., Bampton, M.C.C.: Coupling of substructures for dynamic analyses. AIAA J. **6**(7), 1313–1319 (1968). https://doi.org/10.2514/3.4741
48. Krack, M., Gross, J.: Harmonic Balance for Nonlinear Vibration Problems, vol. 1. Springer International Publishing, Cham (2019). https://doi.org/10.1007/978-3-030-14023-6
49. Cameron, T.M., Griffin, J.H.: An alternating frequency/time domain method for calculating the steady-state response of nonlinear dynamic systems. J. Appl. Mech. **56**(1), 149–154 (1989). https://doi.org/10.1115/1.3176036
50. Siewert, C., Panning, L., Wallaschek, J., Richter, C.: Multiharmonic forced response analysis of a turbine blading coupled by nonlinear contact forces. J. Eng. Gas Turbines Power **132**(8), 082501 (2010). https://doi.org/10.1115/1.4000266
51. Siewert, C., Panning, L., Gerber, C., Masserey, P.A.: Numerical and experimental damping prediction of a nonlinearly coupled low pressure steam turbine blading. In: Proceedings of the ASME Turbo Expo 2008: Power for Land, Sea, and Air. Volume 5: Structures and Dynamics, Parts A and B. Berlin, Germany. pp. 531–542 (2008). https://doi.org/10.1115/GT2008-51073.
52. Chen, J., Zang, C., Zhou, B., Petrov, E.P.: High-fidelity calculation of modal damping caused by friction at blade roots for single blades and tuned bladed disc assemblies. Proc. Inst. Mech. Eng. Part C J. Mech. Eng. Sci. (2020). https://doi.org/10.1177/0954406220935144
53. Byrd, R.H., Hribar, M.E., Nocedal, J.: An interior point algorithm for large-scale nonlinear programming. SIAM J. Optim. **9**(4), 877–900 (1999). https://doi.org/10.1137/S1052623497325107
54. Byrd, R.H., Gilbert, J.C., Nocedal, J.: A trust region method based on interior point techniques for nonlinear programming. Math. Program. **89**, 149–185 (2000). https://doi.org/10.1007/PL00011391